

RESEARCH ARTICLE

Machine-learning-based asymptotic homogenisation and localisation considering boundary layer effects

Xiwei Pan¹  | Zhengcheng Zhou¹  | Chuang Ma¹ | Shaoshuai Li¹ | Yichao Zhu^{1,2}

¹Department of Engineering Mechanics, Dalian University of Technology, Dalian, China

²State Key Laboratory of Structural Analysis, Optimization and CAE Software for Industrial Equipment, Dalian University of Technology, Dalian, China

Correspondence

Yichao Zhu, Department of Engineering Mechanics, Dalian University of Technology, No.2 Linggong Road, Dalian, Liaoning 116024, China.
Email: yichaozhu@dlut.edu.cn

Funding information

National Natural Science Foundation of China, Grant/Award Number: 12172074; Fundamental Research Funds for the Central Universities, P.R. China

Abstract

Asymptotic homogenisation offers a way to efficiently analyse the mechanical behaviour of multiscale configurations. But near a multiscale boundary, the homogenisation strategy should be modified, as the underlying periodicity assumption breaks down there. In this article, we introduce a machine-learning-based asymptotic homogenisation and localisation scheme to formulate such boundary layer effects. To this end, we define a set of boundary layer cells, where external loading conditions are imposed on one side of the cell, and matching conditions with the interior periodic cells are imposed on the opposite side. The formulation is also extended to cover situations where the multi-scale structure is not fully periodic, but spatially varying. Implied from the asymptotic results, neural networks can be trained to memorise the interrelationship between key local quantities, such as the magnitude of the local maximum von Mises stress, and the local mechanical and geometric features. Equipped with the trained neural networks, the online calculation for key (boundary-localised) quantities of interest under arbitrary loading conditions is expected to be accelerated substantially. Numerical examples are further presented to show the reliability of the proposed work for boundary stress prediction.

KEYWORDS

asymptotic homogenisation, boundary layer, localisation, machine learning, multi-scale modelling, surface energy

1 | INTRODUCTION

Configurations decorated with microstructure provide an excellent solution when the issue of lightweight is in concern, and their vast applications have already been seen in engineering fields like aerospace,¹ acoustics,² biomedical applications,³ etc. Over the past few decades, advances in high-performance computing and additive manufacturing keep catalysing the need for multi-scale modelling of materials and systems, and they also put forward requirements for reliable and efficient assessment of the performance of such multi-scale structures for actual service processes.

For multi-scale configurations (MSCs), computation of their localised properties, such as the structural strength and/or the weakest point, still faces challenges. If brute force with extremely fine mesh is carried out directly on multi-scale structures, detailed information of every point is then available. However, this inevitably leads to huge computational costs,^{4,5} some of which may be infeasible for realisation. It is therefore of great practical significance to develop

reliable and efficient multi-scale methods and algorithms, which can properly manage computational efficiency and modelling accuracy. For certain composite multi-scale structures, self-consistent methods, and generalised self-consistent methods provide analytical solutions for a class of simple single inclusion problems. However, for fairly complicated cases, the ideas of treating them as a homogeneous continuum may offer a way out of computational burden. Among them, computational homogenisation (CH) methods rooted in the concept of representative volume element (RVE) have been regarded as a routine operation for analysing MSC.⁶⁻¹⁰ They feature a fairly clear mechanical background and the possibility of dealing with highly complex issues, such as nonlinearity,^{6,7} including large-strain,⁸ heterogeneous materials,¹⁰ etc. Another widely used multi-scale computational strategy stems from the asymptotic homogenisation (AH) method, which links the microscopic characteristics and the equivalent properties through rigorous mathematical derivations, and decomposition of a multi-scale problem into two problems defined on different length scales can be realised. Such an AH way of multi-scale modelling was first devised for the analysis of linear periodic structures^{11,12} and later extended to cover topics of stress-strain nonlinearity,^{13,14} damage,^{15,16} higher-order expansion,¹⁷ and spatially varying microstructure,¹⁸ etc.

All the aforementioned methods enjoy their conceptualised high efficiency in their own fields. But when treating MSCs in a homogenised sense, such homogenisation-based approaches necessitate modification if localised performance indices, such as the strength at the weakest site, are of interest. In the past few decades, cascade of research on CH for local stress recovery have emerged, for example, semi-analytical methods including the Transformation Field Analysis (TFA)^{19,20} and Non-uniform TFA (NTFA),^{21,22} multi-scale computational techniques including the FE² method^{9,23} based on finite element analysis (FEA), methods based on Fast Fourier Transforms,²⁴ and so on. These methods are all proposed for enabling the recovery of the information of localised fields, but often at the cost of suffering from severe efficiency problems.²⁵ For AH approaches, efforts for the recovery of key localised stress components also never cease. Lefik and Schrefler²⁶ pointed out that the homogenisation process will result in two different stress tensors: one is the mean stress field, denoting results of homogenised rather than real structures, and the other is the local stress field, relating to each representative cell. This means that the AH approach is not just limited to giving compliance of MSCs, but can also capture the local behaviour of micro-structures. But such an extraction operation relies on the storage of every cell result and may cause memory explosion when dealing with a large number of micro cells or graded microstructures.

To enhance the efficiency of AH approaches, especially for the extraction of key localised quantities in graded microstructures, a combinative use of machine learning (ML) and AH has been suggested.²⁷ But there remain some problems. Most homogenisation methods, including the mentioned RVE methods, suppose that the object under study extends infinitely along the direction where the cell possesses periodicity, therefore leading to a failure to acquire a good approximation near the boundary of the actual configuration (with a finite size). Moreover, boundaries and interfaces are likely the places where configurational damage initiation begins, thus a scheme to accurately and efficiently capture the localised strength near boundaries should supplement the judgement basis of structural safety. It is generally believed that there are two main reasons why the otherwise reliable AH model in the interior region behaves irregularly near the boundary. Firstly and intuitively, the cell can no longer be deemed to be locally periodic along the boundary normal; secondly, the stress field satisfies a stress boundary condition (BC) not just in a mean sense but a local one. So, due to the presence of such a “boundary layer (BL),” the AH formulation should be modified accordingly.

Earlier attempts on considering BL effects under the AH framework were firstly made in a theoretical way,^{26,28-30} where a “BL corrector” is introduced to the first-order expansion term of the overall displacement field \mathbf{u}^ϵ to take into account the effect of BL on the system. Such an idea of including a BL term to cope with the periodicity loss near a multi-scale boundary was further developed, such as the computation of steady thermal conduction²⁸ and boundary localised stresses for composite materials, such as the stratified materials^{29,30} and superconducting coils.²⁶ Here the “BL corrector” retains periodicity regarding the micro variables tangentially along the boundary, and decays exponentially regarding the microscopic variable along the boundary normal.³¹ Thus the final solution to the global stress field is approximated by the sum of the original AH result and the BL correction term. The idea of BL correctors points out a clear path to capture the characteristic behaviour at multi-scale boundaries, but it also brings with it several limitations for further application

- Existing theoretical studies are mainly focused on periodic structures, where the cell problems to be solved are relatively unitary;
- The boundary shapes they dealt with were all simple cases of straight lines, which may not be easy to implement for configurations with curved boundaries;
- The introduction of “BL corrector” is accompanied with a BL correction problem defined over a domain that is infinitely extended towards the multi-scale interior. This inevitably introduces ambiguities on determining the BL size in computation.

Given the above limitations, tuning the concept of BL corrector in an approximate but computational-friendly manner seems like an intuitive solution. Recently, local stress recovery associated with the BL has been studied from a purely computational aspect based on finite volume element³² and multi-scale eigenelement method.³³ Both of them adopted a two-step strategy, that is, (1) the computation of homogenisation results of the interior region (region except the BL); (2) the reconstruction of the BL using direct FEA, with the original outer BCs and displacements given by interior homogenisation serving as its new BCs. In this paper, we introduce, with regard to fully periodic interior cells, the concept of BL cells that span a limited number (one period to be precise, as systematically investigated by Drago and Pindera³⁴) of constituent cells towards the interior of the porous structure. Instead of demanding exponential decay at infinity, as done in the rigorous treatment, we impose matching conditions of certain stress components on the BL cell boundary that virtually joins with an interior periodic cell. Thus a BL problem can be established, and its predominant discrepancy against an interior cell problem lies in the BCs imposed on surfaces orthogonal to the boundary normal. On the outer boundary of the BL cell, it is imposed with the actual BCs applied to the original MSCs. On the opposite surface, traction BCs in consistency with the virtual interior cell problem are considered. In this viewpoint, a BL cell problem must be in association with an interior cell problem.

The solutions for the BL cell problem mentioned above contain key information about the desired localised stress components, and ML models are trained to store such information. The input arguments of the neural network (NN) in use include the descriptions of the microstructural BL cell, the actual BCs, the on-site mean-field stress, as well as the key parameters summarising the load from the adjacent virtual interior cell problem. Upon the completion of the training of such NNs, the online computation for the homogenised problem suffices as the localised quantities of interest are obtained by just calling the NN with the input arguments evaluated properly.

For method verification, the performance of the NNs constructed above in predicting the local maximum von Mises stresses (LMvMSes) near the structure boundary are examined through several numerical examples, including MSCs with various microstructural geometries and BCs. Two types of NNs are involved here, they are constructed according to the interior cells and BL cells, respectively. Comparison between values predicted by both NNs with the benchmark obtained from the direct fine-mesh FEA of the porous structure shows that the BL networks do give accurate and reliable predictions to the LMvMSes close to the boundary in all the given examples, while in some cases, values predicted by the NN constructed based on the interior cell can also be used as accurate approximations, but they are not 'reliable' though, since the physical model of the interior cell is not reasonable near the edge.

The remainder of this article is structured as follows. The detailed derivation of the BL cell problem subject to displacement BCs in a periodic structure is given in Section 2. Such procedures are further generalised to other cases including stress BCs and spatially varying multi-scale configurations (SVMSC) in Section 3. In Section 4, the specific implementation processes of the ML are introduced on the basis of the obtained asymptotic expressions. And the NNs corresponding to different regions, BCs and geometries are pre-trained. This is followed by the verification, the predicted values are compared with the results given by direct fine-scale computation in Section 5 so as to demonstrate the feasibility and reliability of the present work. A summary and extended discussion comprise of Section 6.

Unless specified, indices with Greek letters, such as α, β , etc., appearing in this article consistently represent the incomplete set of indices excluding that used to capture variation along the boundary normal, that is, $\alpha, \beta = 1, \dots, N - 1$, here N denotes the spatial dimension, while those with Latin letters, such as i, j, k, l, \dots , have a full family of indices from 1 up to N . In addition, the Einstein summation rule is applied to both the Greek indices and the Latin indices throughout the article.

2 | BASIC ASYMPTOTIC FORMULATION OF MICROSTRUCTURAL BOUNDARY LAYER

The current work is aimed to model microstructural BL effects in a more general sense. However, to help the readers be familiarised with the modelling procedure, we are focused on periodic configurations subject to displacement BCs for the moment, and its generalisation will be considered in Section 3.

2.1 | Problem settings

A regular rectangular domain infilled with periodic microstructure in space \mathbb{R}^N , where $N = 2$ or 3 represents the spatial dimension, is considered here in first, with an illustrative example shown in the upper panel of Figure 1. The overall

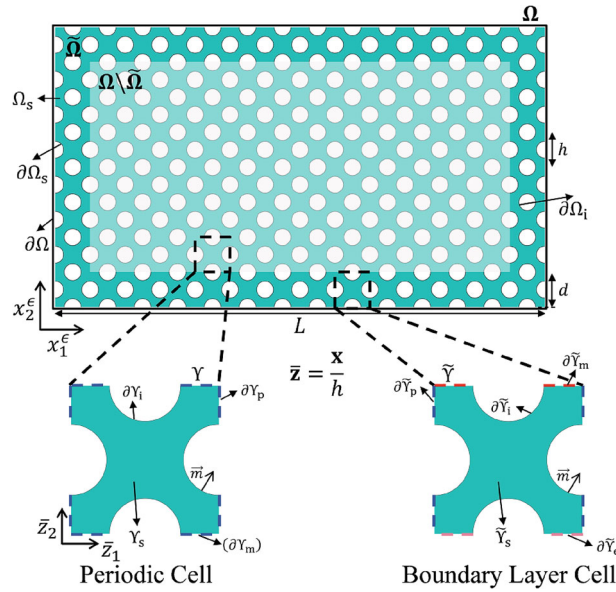


FIGURE 1 Representation of an multi-scale configuration. The whole domain Ω is divided into two parts: the interior region $\Omega \setminus \tilde{\Omega}$ and the boundary layer region $\tilde{\Omega}$.

rectangular domain is denoted by Ω , with $\partial\Omega$ being the corresponding (overall) boundary. Inside Ω , the region occupied by solids is denoted by Ω_s , whose boundary counterpart takes the notation of $\partial\Omega_s$. Thus the actual boundary of this MSC as shown in Figure 1 should consist of two sections. One is the boundary sections in the exterior where external BCs, such as the displacement BC on $\partial\Omega_d$ or the traction BC on $\partial\Omega_t$, can be applied. Mathematically, such boundary sections are contained in the set of

$$\partial\Omega_d \cup \partial\Omega_t = \partial\Omega \cap \partial\Omega_s. \tag{1}$$

The other set of the multi-scale boundary section is formed by boundary pieces in the interior of Ω , that is the inner surface due to the presence of micro-structure, and they are collectively summarised by $\partial\Omega_i$.

A multi-scale structure with an overall characteristic length L is filled in Ω , and its constituent unit cells is characterised by another length parameter h . Given the geometrically multi-scale nature of the configuration, $h \ll L$, and a small parameter ϵ is then introduced by

$$\epsilon = \frac{h}{L} \ll 1. \tag{2}$$

Note that the performance of a multi-scale structure takes place simultaneously at both the macroscopic and the microscopic levels. Here we introduce another coordinate system $x_1^\epsilon - x_2^\epsilon$, where a superscript ‘ ϵ ’ indicates that the spatial variation on both length scales is considered simultaneously.

Therefore, the equilibrium state of the solid part of the MSC is described by

$$-\frac{\partial\sigma_{ij}}{\partial x_j^\epsilon} = f_i, \quad \text{in } \Omega_s, \tag{3}$$

for $i = 1, \dots, N$, where \mathbf{f} is the body force per volume, $\boldsymbol{\sigma}$ is the structural stress field whose components are related to those of the strain field $\boldsymbol{\epsilon}$ through the elasticity tensor $\mathbb{C}_{ijkl}(i, j, k, l = 1, \dots, N)$,

$$\sigma_{ij} = \mathbb{C}_{ijkl}\epsilon_{kl} = \mathbb{C}_{ijkl} \frac{\partial u_k}{\partial x_l^\epsilon}, \tag{4}$$

with \mathbf{u} being the displacement field. Note that the fourth-order tensor possesses a certain symmetry: $\mathbb{C}_{ijkl} = \mathbb{C}_{jikl} = \mathbb{C}_{klij}$.

Meanwhile a set of BCs should be proposed there, together with the governing Equation (3). First, the boundaries from the microstructural interior $\partial\Omega_i$, as illustrated by Figure 1, should be in a traction-free state, that is,

$$\sigma_{ij}m_j = \mathbb{C}_{ijkl} \frac{\partial u_k}{\partial x_l^\epsilon} m_j \Big|_{\partial\Omega_i} = 0. \quad (5)$$

On the microstructural exterior, we are focused in this section on displacement BCs given by

$$u_i|_{\partial\Omega_d} = u_i^0. \quad (6)$$

2.2 | Asymptotic expansion

2.2.1 | Introduction of boundary layer cells

The fundamental assumption of micro-structures being locally periodic underlying general AH theory becomes questionable near the domain boundary. To this end, we consider a layer of “special cells” (termed as the BL cells) connecting the interior with the actual boundary. As shown in Figure 1, the geometry of such BL cells can be identical or slightly different from the interior cells. Note that there are certain scenarios where cells near the domain boundary bear different geometric profiles against the cells in the interior for practical purpose. For instance, a solid frame is usually attached to the periphery of an MSC to facilitate the external loadings.

Due to the presence of such BLs, the computational domain is divided into two parts: the interior region $\Omega \setminus \tilde{\Omega}$ and the BL region $\tilde{\Omega}$. Here the symbol “ \sim ” is used to distinguish quantities evaluated in the BL from those in the interior, and the BL thickness is set to be d . Aiming to capture the “multi-scale” feature of the model, non-dimensionalisation is carried out for spatial variables and some other quantities, that is,

$$\bar{\mathbf{x}}^\epsilon = \frac{\mathbf{x}^\epsilon}{L}, \quad \bar{\mathbf{u}} = \frac{\mathbf{u}}{L}, \quad \bar{\mathbb{C}}_{ijkl} = \frac{\mathbb{C}_{ijkl}}{\mathbb{C}_{1111}}, \quad (7)$$

where L is recalled to be the length of the specimen, the “ $\bar{\cdot}$ ” symbol over a letter denotes its non-dimensional counterpart, and the meaning of which will be consistent in the subsequent derivation.

To further investigate the influence of microstructure, we amplify the original scale variables by dividing the cell length to create a coordinate system $\bar{z}_1 - \bar{z}_2$ in the microscopic scale, and the corresponding variable $\bar{\mathbf{z}}$ is thus defined by

$$\bar{\mathbf{z}} = \frac{\mathbf{x}}{h} = \frac{\bar{\mathbf{x}}}{\epsilon}. \quad (8)$$

Therefore, the original periodic cell domain is non-dimensionalised to $\Upsilon = [0, 1]^N$, and the BL cell becomes $\tilde{\Upsilon} = [0, 1]^{N-1} \times [0, \zeta]$, where the non-dimensional BL thickness equals

$$\zeta = d/h. \quad (9)$$

Inside the two types of cells, the solid regions are denoted by Υ_s and $\tilde{\Upsilon}_s$, respectively, with $\partial\Upsilon_s$ and $\partial\tilde{\Upsilon}_s$ being the corresponding solid boundaries.

Here without loss of generalities, we can assume that the boundary section for BL consideration always coincides with the $x_N = 0$ line/plane. Once boundary sections which are located at different places or with a different boundary orientation are under investigation, one may refer to Appendix A to see the linkage between the formulation then and the present situation.

Compared with the interior cells, a BL cell accommodates more various BCs. Here a noting subindex is affiliated with a boundary section in the BL cell $\tilde{\Upsilon}$, so as to indicate the type of BCs imposed there, and they are illustrated in the bottom left panel of Fig. 1 and get summarised as follows. $\partial\tilde{\Upsilon}_p$ indicates the periodic boundary that is a part of the cell exterior boundary orthogonal to the local tangent plane at the on-site boundary point; $\partial\tilde{\Upsilon}_m$ indicates the boundary section where a matching of traction BCs with a virtual interior cell is required; $\partial\tilde{\Upsilon}_e$ denotes the boundary

section that coincides with the actual BC applied to the overall domain; $\partial\tilde{\Upsilon}_i$ denotes the interior boundary section within $\tilde{\Upsilon}$ where a traction-free state is declared. And \mathbf{m} represents the outer normal at a point on the boundary of a cell entity.

2.2.2 | Asymptotic formulation with the interior cell

The treatment of the original Equation (3) in the interior cell Υ is the same as that in traditional AH models, that is, one can consider its asymptotic behaviour in a scale-separated form. Thus, the two-scale variable \bar{x}_i^ϵ can be expressed as two terms related to a set of macroscopic variable \bar{x}_i and the set of microscopic variable \bar{z}_i defined by Equation (8). It is noted that scale separation emerges as the spatial gradient with respect to \bar{x}^ϵ is considered. Upon the use of the differentiation chain rule, we have

$$\frac{\partial}{\partial \bar{x}_i^\epsilon} = \frac{\partial}{\partial \bar{x}_i} + \frac{1}{\epsilon} \frac{\partial}{\partial \bar{z}_i}. \quad (10)$$

Note that the AH formulation over the periodic cell has been discussed properly in literature, for example, Reference 11. Here we just list the key results for further usage.

- 1) The asymptotic expansion of the displacement and stress fields in terms of the small parameter ϵ reads

$$\bar{u}_i^\epsilon \sim \bar{u}_i^{(0)}(\bar{\mathbf{x}}) + \epsilon \bar{u}_i^{(1)}(\bar{\mathbf{x}}; \bar{\mathbf{z}}) + \dots \sim \bar{u}_i^H(\bar{\mathbf{x}}) + \epsilon \left(\xi_i^{st} \frac{\partial \bar{u}_s^H}{\partial \bar{x}_t} \right) + \mathcal{O}(\epsilon^2); \quad (11a)$$

$$\bar{\sigma}_{ij} \sim \bar{\sigma}_{ij}^{(0)} + \epsilon \bar{\sigma}_{ij}^{(1)} + \dots \sim \left(\bar{\mathbb{C}}_{ijkl} + \bar{\mathbb{C}}_{ijst} \frac{\partial \xi_s^{kl}}{\partial \bar{z}_t} \right) \frac{\partial \bar{u}_k^H}{\partial \bar{x}_l} + \mathcal{O}(\epsilon), \quad (11b)$$

where $\bar{\mathbf{u}}^H$ denotes the (non-dimensional) homogenised displacement field; ξ_i^{st} form a third-order tensor which is the solution of certain cell problems defined on the interior periodic cell.

- (2) The equivalent macroscopic elasticity tensor of the periodic cell is formed by

$$\bar{\mathbb{C}}_{ijkl}^H = \int_{\Upsilon_s} \left(\bar{\mathbb{C}}_{ijkl} + \bar{\mathbb{C}}_{ijst} \frac{\partial \xi_s^{kl}}{\partial \bar{z}_t} \right) d\bar{\mathbf{z}}. \quad (12)$$

- (3) A homogenised equilibrium equation for $\bar{\mathbf{u}}^H$ of the interior region is established by

$$\frac{\partial}{\partial \bar{x}_j} \left(\bar{\mathbb{C}}_{ijkl}^H \frac{\partial \bar{u}_k^H}{\partial \bar{x}_l} \right) = 0, \quad \text{in } \bar{\Omega} \setminus \bar{\Omega}. \quad (13)$$

2.2.3 | Expansion of the field variables in the BL region

Due to the absence of periodicity along the surface normal, the structural behaviour in the BL region should be analysed exclusively, while its matching with the interior cell needs to be taken into account. In the BL region, the geometric domain of the BL cell can be expressed as $\partial\bar{\Omega} \times \tilde{\Upsilon}$, with $\partial\bar{\Omega} = \{\bar{\mathbf{x}} | \bar{x}_N = 0\}$. Note that on $\partial\bar{\Omega}$, differentiation is only meaningful along any direction in perpendicular to the on-site surface normal. As a result, the term $\partial/\partial \bar{x}_N$ should no longer appear as the scale get separated, that is,

$$\frac{\partial}{\partial \bar{x}_\alpha^\epsilon} = \frac{\partial}{\partial \bar{x}_\alpha} + \frac{1}{\epsilon} \frac{\partial}{\partial \bar{z}_\alpha}; \quad \frac{\partial}{\partial \bar{x}_N^\epsilon} = \frac{1}{\epsilon} \frac{\partial}{\partial \bar{z}_N}. \quad (14)$$

It is recalled that the Greek subindex α here is adopted implying that consideration is only for the $(N - 1)$ variables that are parallel to the on-site tangent plane. In the BL region, variation along the surface normal is merely due to

TABLE 1 Asymptotic expansion in both the interior and the BL regions as shown in Figure 1.

| | Interior region | Boundary layer region |
|------------|--|---|
| Rescale | $\bar{\mathbf{z}} = \bar{\mathbf{x}}/\epsilon$ | $\bar{\mathbf{z}} = \bar{\mathbf{x}}/\epsilon$ |
| Free | $\bar{x}_i \in \bar{\Omega} \setminus \bar{\Omega}, \bar{z}_i \in \Upsilon_s$ | $\bar{x}_\alpha \in \bar{\Omega}, \bar{z}_i \in \tilde{\Upsilon}_s$ |
| Variables | $i = 1, \dots, N$ | $\alpha = 1, \dots, N-1; i = 1, \dots, N$ |
| Scale | $\frac{\partial}{\partial \bar{x}_i} = \frac{\partial}{\partial x_i} + \frac{1}{\epsilon} \frac{\partial}{\partial \bar{z}_i}$ | $\frac{\partial}{\partial \bar{x}_\alpha} = \frac{\partial}{\partial x_\alpha} + \frac{1}{\epsilon} \frac{\partial}{\partial \bar{z}_\alpha}$ |
| Separation | | $\frac{\partial}{\partial \bar{x}_N} = \frac{1}{\epsilon} \frac{\partial}{\partial \bar{z}_N}$ |

the micro-structural presence measured in \bar{z}_N . Therefore, the displacement and stress fields in the BL region should be asymptotically expanded by

$$\begin{aligned} \bar{u}_i^\epsilon &\sim \bar{u}_i^{(0)}(\bar{x}_\alpha, 0; \bar{\mathbf{z}}) + \epsilon \bar{u}_i^{(1)}(\bar{x}_\alpha, 0; \bar{\mathbf{z}}) + \dots; \\ \bar{\sigma}_{ij} &\sim \frac{1}{\epsilon} \bar{\sigma}_{ij}^{(-1)} + \bar{\sigma}_{ij}^{(0)} + \dots = \frac{1}{\epsilon} \bar{C}_{ijkl} \frac{\partial \bar{u}_k^{(0)}}{\partial \bar{z}_l} + \bar{C}_{ijk\alpha} \frac{\partial \bar{u}_k^{(0)}}{\partial \bar{x}_\alpha} + \bar{C}_{ijkl} \frac{\partial \bar{u}_k^{(1)}}{\partial \bar{z}_l} + \dots, \end{aligned} \quad (15)$$

respectively, where $i, j, k, l = 1, \dots, N; \alpha = 1, \dots, N-1; (\bar{\mathbf{x}}, \bar{\mathbf{z}}) \in \bar{\Omega} \times \tilde{\Upsilon}_s$.

In Table 1, the scale separation formulas in the interior and the BL region are summarised in a comparative manner.

2.3 | Asymptotic analysis of the boundary layer effects

Now the asymptotic behaviour of Equation (3) in the BL region $\bar{\Omega}$ is investigated. For simplicity, we temporarily neglect the role of the body force \mathbf{f} .

2.3.1 | Leading-order formulation: preparation

At the leading order ($\mathcal{O}(1/\epsilon^2)$), all conditions on the boundary sections of $\tilde{\Upsilon}_s$ should be homogeneous, because the loads applied never exceeds $\mathcal{O}(1)$. Therefore, the cell problem at $\mathcal{O}(1/\epsilon^2)$ is obtained as

$$\left\{ \begin{aligned} \frac{\partial \bar{\sigma}_{ij}^{(-1)}}{\partial \bar{z}_j} &= \frac{\partial}{\partial \bar{z}_j} \left(\bar{C}_{ijkl} \frac{\partial \bar{u}_k^{(0)}}{\partial \bar{z}_l} \right) = 0, \text{ in } \tilde{\Upsilon}_s; \end{aligned} \right. \quad (16a)$$

$$\bar{C}_{ijkl} \frac{\partial \bar{u}_k^{(0)}}{\partial \bar{z}_l} m_j \Big|_{\partial \tilde{\Upsilon}_i} = 0; \quad (16b)$$

$$\bar{u}_i^{(0)}, \frac{\partial \bar{u}_i^{(0)}}{\partial \bar{z}_j} \text{ periodic on } \partial \tilde{\Upsilon}_p; \quad (16c)$$

$$\bar{C}_{ijkl} \frac{\partial \bar{u}_k^{(0)}}{\partial \bar{z}_l} m_j \Big|_{\partial \tilde{\Upsilon}_m} = \bar{C}_{ijk\alpha} \frac{\partial \bar{u}_k^{(0)}}{\partial \bar{x}_\alpha} m_j \Big|_{\partial \Upsilon_m} = 0; \quad (16d)$$

$$\bar{u}_i^{(0)} \Big|_{\partial \tilde{\Upsilon}_e} = \bar{u}_i^0. \quad (16e)$$

It can be verified with ease that for problem (16) to hold, the zero-order displacement field of BL $\bar{u}_i^{(0)}$ should be independent of $\bar{\mathbf{z}}$, that is,

$$\bar{u}_i^{(0)}(\bar{\mathbf{x}}; \bar{\mathbf{z}}) = \bar{u}_i^{(0)}(\bar{\mathbf{x}}). \quad (17)$$

Compared with the expansion for the inner displacement field given by Equation (11a), Equation (17) implies that the leading-order displacement of the interior region can be naturally extended to the domain boundary, that is,

$$\bar{u}_i^{(0)} \Big|_{\bar{x}_N=0} = \bar{u}_i^{(0)}. \quad (18)$$

2.3.2 | First-order formulation: derivation of BL cell problems

At the first order ($\mathcal{O}(1/\epsilon)$), the BL formulation is established in regard with the interior cell it joins with, as shown in Figure 2. With the BCs on different sections of the BL cell $\tilde{\Upsilon}$ identified, the problem describing the force-equilibrated state at $\mathcal{O}(1/\epsilon)$ in the BL cell reads

$$\left\{ \begin{array}{l} \frac{\partial \bar{\sigma}_{ij}^{(0)}}{\partial \bar{z}_j} = \frac{\partial}{\partial \bar{z}_j} \left(\bar{\mathbb{C}}_{ijk\alpha} \frac{\partial \bar{u}_k^{(0)}}{\partial \bar{x}_\alpha} + \bar{\mathbb{C}}_{ijkl} \frac{\partial \bar{u}_k^{(1)}}{\partial \bar{z}_l} \right) = 0, \text{ in } \tilde{\Upsilon}_s; \quad (19a) \\ \left(\bar{\mathbb{C}}_{ijk\alpha} \frac{\partial \bar{u}_k^{(0)}}{\partial \bar{x}_\alpha} + \bar{\mathbb{C}}_{ijkl} \frac{\partial \bar{u}_k^{(1)}}{\partial \bar{z}_l} \right) m_j \Big|_{\partial \tilde{\Upsilon}_i} = 0; \quad (19b) \\ \bar{u}_i^{(1)}, \frac{\partial \bar{u}_i^{(1)}}{\partial \bar{z}_j} \text{ periodic on } \partial \tilde{\Upsilon}_p; \quad (19c) \\ \left(\bar{\mathbb{C}}_{ijk\alpha} \frac{\partial \bar{u}_k^{(0)}}{\partial \bar{x}_\alpha} + \bar{\mathbb{C}}_{ijkl} \frac{\partial \bar{u}_k^{(1)}}{\partial \bar{z}_l} \right) m_j \Big|_{\partial \tilde{\Upsilon}_m} = \bar{\sigma}_{ij}^{(0)} m_j \Big|_{\partial \Upsilon_m}; \quad (19d) \\ \bar{u}_i^{(1)} \Big|_{\partial \tilde{\Upsilon}_e} = 0. \quad (19e) \end{array} \right.$$

It can be verified that the solution for problem (19) should take the form of

$$\bar{u}_i^{(1)} = \bar{\xi}_i^{sa} \frac{\partial \bar{u}_s^{(0)}}{\partial \bar{x}_\alpha} + \bar{\eta}_i^{st} \frac{\partial \bar{u}_s^{(0)}}{\partial \bar{x}_t}, \quad (20)$$

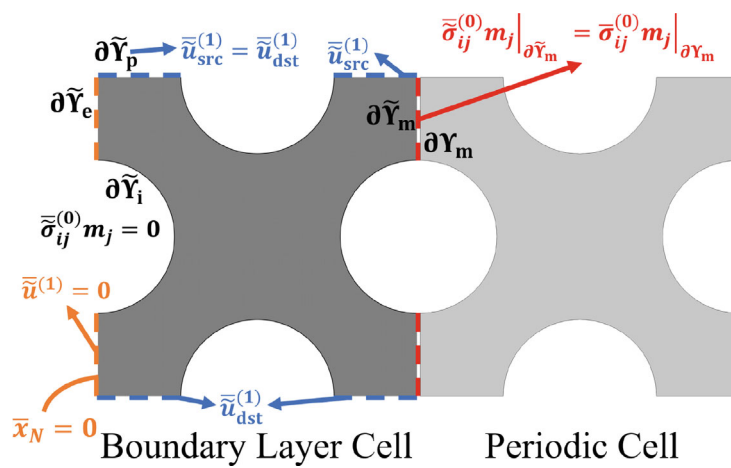


FIGURE 2 Demonstration of the actual boundary conditions (BCs) associated with a boundary layer (BL) cell on the left edge of the multi-scale configuration. The boundaries of voids interior are represented by the notation $\partial \tilde{\Upsilon}_i$, on which traction-free BC (19b) is imposed; the upper and lower ones marked in blue represents periodic boundaries (19c) on $\partial \tilde{\Upsilon}_p$; the boundary section on the right side of the BL cell, as marked in red, represents the boundary $\partial \tilde{\Upsilon}_m$, on which matching condition with the interior cell is imposed, that is, Equation (19d); the boundary section on the left side of $\tilde{\Upsilon}$ in yellow represents the outer boundary $\partial \tilde{\Upsilon}_e$, which is set to be fixed here, that is, Equation (19e).

for $i = 1, \dots, N$, where the two third-order tensors $\tilde{\xi}$ and $\tilde{\eta}$ satisfy

$$\left\{ \begin{array}{l} \frac{\partial}{\partial \bar{z}_j} \left(\bar{C}_{ijk\alpha} \delta_{ks} \delta_{\alpha\beta} + \bar{C}_{ijkl} \frac{\partial \tilde{\xi}_k^{s\beta}}{\partial \bar{z}_l} \right) = 0, \text{ in } \tilde{Y}_s; \end{array} \right. \quad (21a)$$

$$\left\{ \begin{array}{l} \left(\bar{C}_{ijk\alpha} \delta_{ks} \delta_{\alpha\beta} + \bar{C}_{ijkl} \frac{\partial \tilde{\xi}_k^{s\beta}}{\partial \bar{z}_l} \right) m_j \Big|_{\partial \tilde{Y}_i} = 0; \end{array} \right. \quad (21b)$$

$$\left\{ \begin{array}{l} \tilde{\xi}_i^{s\beta}, \frac{\partial \tilde{\xi}_i^{s\beta}}{\partial \bar{z}_j} \text{ periodic on } \partial \tilde{Y}_p; \end{array} \right. \quad (21c)$$

$$\left\{ \begin{array}{l} \left(\bar{C}_{ijk\alpha} \delta_{ks} \delta_{\alpha\beta} + \bar{C}_{ijkl} \frac{\partial \tilde{\xi}_k^{s\beta}}{\partial \bar{z}_l} \right) m_j \Big|_{\partial \tilde{Y}_m} = 0; \end{array} \right. \quad (21d)$$

$$\left\{ \begin{array}{l} \tilde{\xi}_i^{s\beta} \Big|_{\partial \tilde{Y}_e} = 0, \end{array} \right. \quad (21e)$$

and

$$\left\{ \begin{array}{l} \frac{\partial}{\partial \bar{z}_j} \left(\bar{C}_{ijkl} \frac{\partial \tilde{\eta}_k^{st}}{\partial \bar{z}_l} \right) = 0, \text{ in } \tilde{Y}_s; \end{array} \right. \quad (22a)$$

$$\left\{ \begin{array}{l} \bar{C}_{ijkl} \frac{\partial \tilde{\eta}_k^{st}}{\partial \bar{z}_l} m_j \Big|_{\partial \tilde{Y}_i} = 0; \end{array} \right. \quad (22b)$$

$$\left\{ \begin{array}{l} \tilde{\eta}_i^{st}, \frac{\partial \tilde{\eta}_i^{st}}{\partial \bar{z}_j} \text{ periodic on } \partial \tilde{Y}_p; \end{array} \right. \quad (22c)$$

$$\left\{ \begin{array}{l} \bar{C}_{ijkl} \frac{\partial \tilde{\eta}_k^{st}}{\partial \bar{z}_l} m_j \Big|_{\partial \tilde{Y}_m} = \left(\bar{C}_{ijst} + \bar{C}_{ijkl} \frac{\partial \xi_k^{st}}{\partial \bar{z}_l} \right) m_j \Big|_{\partial \tilde{Y}_m}; \end{array} \right. \quad (22d)$$

$$\left\{ \begin{array}{l} \tilde{\eta}_i^{st} \Big|_{\partial \tilde{Y}_e} = 0, \end{array} \right. \quad (22e)$$

respectively.

Equation (20) expresses $\bar{u}_i^{(1)}$, the displacement field in the BL region, as the superposition of two terms, each one is given by means of the product of a function solely on \bar{x} and the component of a third-order tensor to be solved for. Here problems (21) and (22) are collectively called the BL cell problems. To guarantee uniqueness of the solutions for the above two BL cell problems, a zero-mean condition is applied to both $\tilde{\xi}$ and $\tilde{\eta}$, that is,

$$\int_{\tilde{Y}_s} \tilde{\xi}_i^{s\alpha} d\bar{z} = 0, \quad \int_{\tilde{Y}_s} \tilde{\eta}_i^{st} d\bar{z} = 0. \quad (23)$$

It is noted that Equation (21) defines a boundary value problem as such: an equilibrated BL cell with fixed outer boundary $\partial \tilde{Y}_e$, a traction-free BC on the opposite side and periodic BCs on the other two sides. While for the BL cell problem (22), the matching conditions (22d) of certain stress components with the virtual interior cell have to be considered on boundary $\partial \tilde{Y}_m$, rather than a traction-free one.

With Equations (20), (21), and (22), the leading-order stress distribution of the BL cell is expressed by

$$\bar{\sigma}_{ij}^{(0)} = \left(\bar{C}_{ijk\alpha} + \bar{C}_{ijst} \frac{\partial \xi_s^{k\alpha}}{\partial \bar{z}_t} \right) \frac{\partial \bar{u}_k^{(0)}}{\partial \bar{x}_\alpha} + \bar{C}_{ijst} \frac{\partial \tilde{\eta}_s^{kl}}{\partial \bar{z}_t} \frac{\partial \bar{u}_k^{(0)}}{\partial \bar{x}_l}. \quad (24)$$

It should be made clear that we here only consider the continuity of unknowns in two regions up to $\mathcal{O}(\epsilon)$.

2.3.3 | Second-order formulation: homogenisation

At the second order ($\mathcal{O}(1)$), the homogenisation is conducted in the BL region. This is done by firstly writing down the force-equilibrium equation at $\mathcal{O}(1)$, that is,

$$\frac{\partial \bar{\sigma}_{i\alpha}^{(0)}}{\partial \bar{x}_\alpha} + \frac{\partial \bar{\sigma}_{ij}^{(1)}}{\partial \bar{z}_j} = 0. \quad (25)$$

Integrating Equation (25) with respect to the micro variable $\bar{\mathbf{z}}$ over the solid domain $\tilde{\Upsilon}_s$, gives

$$\frac{\partial}{\partial \bar{x}_\alpha} \int_{\tilde{\Upsilon}_s} \bar{\sigma}_{i\alpha}^{(0)} d\bar{\mathbf{z}} + \int_{\tilde{\Upsilon}_s} \frac{\partial \bar{\sigma}_{ij}^{(1)}}{\partial \bar{z}_j} d\bar{\mathbf{z}} = 0. \quad (26)$$

The second term on the left of Equation (26) can be transformed into a boundary integral with the use of Green's formula, that is,

$$\int_{\tilde{\Upsilon}_s} \frac{\partial \bar{\sigma}_{ij}^{(1)}}{\partial \bar{z}_j} d\bar{\mathbf{z}} = \int_{\partial \tilde{\Upsilon}_i + \partial \tilde{\Upsilon}_p + \partial \tilde{\Upsilon}_e + \partial \tilde{\Upsilon}_m} \bar{\sigma}_{ij}^{(1)} m_j dS, \quad (27)$$

where dS is the infinitesimal arclength/area taken from the cell boundary.

Several remarks are noted regarding Equation (27). Firstly, as stated in Section 2.1, no traction or pressure will be imposed from the void interiors, so the integral on boundary $\partial \tilde{\Upsilon}_i$ should vanish. Secondly, the local-periodicity assumption indicates that the integral on boundary $\partial \tilde{\Upsilon}_p$ also vanishes. Thirdly, sum of the last two integral terms is zero due to the $\mathcal{O}(\varepsilon)$ force balance condition on two opposite boundaries, that is, the total force applied on the outer boundary $\partial \tilde{\Upsilon}_e$ should be balanced with the total force due to the virtual interior cell. As a result, the boundary integral on the right side of Equation (27) vanishes, thus the second term on the left of Equation (26) equals zero eventually, that is,

$$\frac{\partial}{\partial \bar{x}_\alpha} \int_{\tilde{\Upsilon}_s} \bar{\sigma}_{i\alpha}^{(0)} d\bar{\mathbf{z}} = 0. \quad (28)$$

Incorporating Equation (24) into Equation (28) gives

$$\frac{\partial}{\partial \bar{x}_\alpha} \left[\frac{\partial \bar{u}_k^{(0)}}{\partial \bar{x}_\beta} \int_{\tilde{\Upsilon}_s} \left(\bar{\mathbb{C}}_{iak\beta} + \bar{\mathbb{C}}_{ia\alpha t} \frac{\partial \bar{\xi}_s^{k\beta}}{\partial \bar{z}_t} \right) d\bar{\mathbf{z}} + \frac{\partial \bar{u}_k^{(0)}}{\partial \bar{x}_l} \int_{\tilde{\Upsilon}_s} \bar{\mathbb{C}}_{ia\alpha t} \frac{\partial \bar{\eta}_s^{kl}}{\partial \bar{z}_t} d\bar{\mathbf{z}} \right] = 0, \text{ on } \partial \bar{\Omega}. \quad (29)$$

If we further define

$$\bar{\mathbb{C}}_{iak\beta}^H = \int_{\tilde{\Upsilon}_s} \left(\bar{\mathbb{C}}_{iak\beta} + \bar{\mathbb{C}}_{ia\alpha t} \frac{\partial \bar{\xi}_s^{k\beta}}{\partial \bar{z}_t} + \bar{\mathbb{C}}_{ia\alpha t} \frac{\partial \bar{\eta}_s^{k\beta}}{\partial \bar{z}_t} \right) d\bar{\mathbf{z}}, \quad (30a)$$

$$\bar{\mathbb{C}}_{ijkN}^H = \int_{\tilde{\Upsilon}_s} \bar{\mathbb{C}}_{ij\alpha t} \frac{\partial \bar{\eta}_s^{kN}}{\partial \bar{z}_t} d\bar{\mathbf{z}}, \quad (30b)$$

Equation (29) can be simplified as

$$\frac{\partial}{\partial \bar{x}_\alpha} \left(\bar{\mathbb{C}}_{iak\beta}^H \frac{\partial \bar{u}_k^H}{\partial \bar{x}_\beta} + \bar{\mathbb{C}}_{iakN}^H \frac{\partial \bar{u}_k^H}{\partial \bar{x}_N} \right) = 0, \text{ on } \partial \bar{\Omega}, \quad (31)$$

where the indices $\alpha, \beta = 1, \dots, N-1$.

Note that $\bar{\mathbb{C}}_{iakl}^H$ defined through Equations (30) play a same role as the surface elasticity moduli introduced in classical Gurtin–Murdoch surface elasticity theory.^{35,36} Several issues should be mentioned in regards. Firstly, from their subindices, it can be observed that the range of the second index $\alpha = 1, \dots, N-1$ differs from that of its other indices

$i, k, l = 1, \dots, N$. Hence $\bar{\mathbb{C}}_{iakl}^H$ bear $N^3 \times (N-1)$ entries, distinguishing it from the normal fourth-order elasticity tensor defined in the domain interior. Secondly, the (non-dimensional) surface elasticity coefficients (SEC) $\bar{\mathbb{C}}_{iakl}^H$ also bear certain symmetry about the components, but only in the plane tangent to the overall domain boundary. Thirdly, experimental evaluation of the SEC still faces difficulties for the moment, but suggestions on their numerical evaluation upon homogenising the underlying atomic structures have been proposed.³⁷

Equation (31) offers to describe the actual force-equilibrium state in the vicinity of the multi-scale boundary. It is an equation defined on a manifold, which may bring about difficulties in finding its numerical solutions, especially when the profile of the boundary is of certain degree of complexities.

2.4 | Energy formulation

The multi-scale behaviour formulated as above can also be studied from a perspective of system energy. Firstly, for a deformed multi-scale body in elastic stage, its (non-dimensional) strain energy is defined by

$$\bar{\mathcal{U}} = \frac{1}{2} \int_{\bar{\Omega}} \bar{\sigma}_{ij} \frac{\partial \bar{u}_i}{\partial \bar{x}_j} d\bar{\mathbf{x}}^e, \quad (32)$$

where the superscript ‘ e ’ implies the corresponding variable links both the macro and micro variables. In the context of homogenisation, integration over a multi-scale domain, with Equation (32) being an example, can be reformulated in a scale-separated manner.³⁸ It relies on an asymptotic formula of

$$\lim_{\epsilon \rightarrow 0} \int_{\bar{\Omega} \setminus \bar{\Omega}} h^\epsilon(\bar{\mathbf{x}}^\epsilon) d\bar{\mathbf{x}}^\epsilon = \int_{\bar{\Omega} \setminus \bar{\Omega}} \int_{\Upsilon} h^{(0)}(\bar{\mathbf{x}}; \bar{\mathbf{z}}) d\bar{\mathbf{z}} d\bar{\mathbf{x}}, \quad (33)$$

where $h^\epsilon(\bar{\mathbf{x}}^\epsilon)$ is the original quasi-periodic function, and $h^{(0)}(\bar{\mathbf{x}}; \bar{\mathbf{z}})$ is the leading-order for its two-scale expansion.

In a similar sense, the idea can be generalised to an asymptotic formula associated with the BL, that is,

$$\lim_{\epsilon \rightarrow 0} \int_{\bar{\Omega}} h^\epsilon(\bar{\mathbf{x}}^\epsilon) d\bar{\mathbf{x}}^\epsilon = \int_{\partial \bar{\Omega}} \delta \int_{\tilde{\Upsilon}} h^{(0)}(\bar{\mathbf{x}}; \bar{\mathbf{z}}) d\bar{\mathbf{z}} dS_{\bar{\mathbf{x}}}, \quad (34)$$

where $\delta = d/L$ is the non-dimensional thickness of the BL, $dS_{\bar{\mathbf{x}}}$ represents the infinitesimal arclength on boundary $\partial \bar{\Omega}$. A short bar added to the integral sign indicates the result is averaged over the integration domain: $f_{\Upsilon} h(\bar{\mathbf{x}}; \bar{\mathbf{z}}) d\bar{\mathbf{z}} = \frac{1}{|\Upsilon|} \int_{\Upsilon} h(\bar{\mathbf{x}}; \bar{\mathbf{z}}) d\bar{\mathbf{z}}$, with $|\Upsilon|$ being the area or volume of the analysed cell.

With Equation (34), one can calculate the elastic energy in the vicinity of the overall MSC boundary in two steps. First, the (homogenised) elastic energy density is calculated through integrals over the BL cell. Note that upon integration over the BL cell, the obtained quantity becomes homogenised and is defined merely on the macroscopic boundary. Therefore, this energy density quantity is effectively the surface energy density. Then the system surface energy should be calculated by integrating the surface energy density over the whole surface $\partial \bar{\Omega}$.

Equipped with such strategy, we can combining Equations (32) and (33) to get the $\mathcal{O}(1)$ approximation of (non-dimensional) energy formulation due to the interior region

$$\bar{\mathcal{U}}_{\text{in}} \approx \frac{1}{2} \int_{\bar{\Omega} \setminus \bar{\Omega}} \int_{\Upsilon_s} \bar{\sigma}_{ij}^{(0)} \left(\frac{\partial \bar{u}_i^{(0)}}{\partial \bar{x}_j} + \frac{\partial \xi_i^{st}}{\partial \bar{z}_j} \frac{\partial \bar{u}_s^{(0)}}{\partial \bar{x}_t} \right) d\bar{\mathbf{z}} d\bar{\mathbf{x}}. \quad (35)$$

Note that the second term on the right of Equation (35) can be eliminated by using the BCs and $\mathcal{O}(1/\epsilon)$ equilibrium equation, that is,

$$\int_{\Upsilon_s} \bar{\sigma}_{ij}^{(0)} \frac{\partial \xi_i^{st}}{\partial \bar{z}_j} \frac{\partial \bar{u}_s^{(0)}}{\partial \bar{x}_t} d\bar{\mathbf{z}} = \frac{\partial \bar{u}_s^{(0)}}{\partial \bar{x}_t} \left(\int_{\partial \Upsilon_1 + \partial \Upsilon_p} \bar{\sigma}_{ij}^{(0)} m_j \xi_i^{st} dS - \int_{\Upsilon_s} \frac{\partial \bar{\sigma}_{ij}^{(0)}}{\partial \bar{z}_j} \xi_i^{st} d\bar{\mathbf{z}} \right) = 0. \quad (36)$$

Thus the non-dimensional leading-order elastic energy due to the domain interior is calculated by

$$\bar{U}_{\text{in}} \approx \frac{1}{2} \int_{\bar{\Omega} \setminus \bar{\Omega}} \int_{\bar{\Gamma}_s} \bar{\sigma}_{ij}^{(0)} \, d\bar{\mathbf{z}} \frac{\partial \bar{u}_i^{(0)}}{\partial \bar{x}_j} \, d\bar{\mathbf{x}} = \frac{1}{2} \int_{\bar{\Omega} \setminus \bar{\Omega}} \bar{\mathbb{C}}_{ijkl}^{\text{H}} \frac{\partial \bar{u}_i^{(0)}}{\partial \bar{x}_j} \frac{\partial \bar{u}_k^{(0)}}{\partial \bar{x}_l} \, d\bar{\mathbf{x}}. \quad (37)$$

The leading-order non-dimensional elastic energy due to the BL region can also be calculated with reference to Equation (34), that is,

$$\begin{aligned} \bar{U}_{\text{b}} &\approx \frac{\delta}{2} \int_{\partial \bar{\Omega}_d} \int_{\bar{\Gamma}_s} \left(\bar{\sigma}_{i\alpha}^{(0)} \frac{\partial \bar{u}_i^{(0)}}{\partial \bar{x}_\alpha} + \bar{\sigma}_{ij}^{(0)} \frac{\partial \bar{u}_i^{(1)}}{\partial \bar{z}_j} \right) \, d\bar{\mathbf{z}} \, dS_{\bar{\mathbf{x}}} \\ &= \frac{\delta}{2} \int_{\partial \bar{\Omega}_d} \int_{\bar{\Gamma}_s} \left(\bar{\sigma}_{i\alpha}^{(0)} \frac{\partial \bar{u}_i^{(0)}}{\partial \bar{x}_\alpha} + \bar{\sigma}_{ij}^{(0)} \frac{\partial \bar{\xi}_i^{\text{sa}}}{\partial \bar{z}_j} \frac{\partial \bar{u}_s^{(0)}}{\partial \bar{x}_\alpha} + \bar{\sigma}_{ij}^{(0)} \frac{\partial \bar{\eta}_i^{\text{st}}}{\partial \bar{z}_j} \frac{\partial \bar{u}_s^{(0)}}{\partial \bar{x}_t} \right) \, d\bar{\mathbf{z}} \, dS_{\bar{\mathbf{x}}}, \end{aligned} \quad (38)$$

similar as in the operation of Equation (36), the two integral terms concerning $\bar{\xi}$ and $\bar{\eta}$ can be further simplified by

$$\int_{\bar{\Gamma}_s} \bar{\sigma}_{ij}^{(0)} \frac{\partial \bar{\xi}_i^{\text{sa}}}{\partial \bar{z}_j} \frac{\partial \bar{u}_s^{(0)}}{\partial \bar{x}_\alpha} \, d\bar{\mathbf{z}} = \frac{\partial \bar{u}_s^{(0)}}{\partial \bar{x}_\alpha} \int_{\partial \bar{\Gamma}_m} \bar{\sigma}_{ij}^{(0)} m_j \bar{\xi}_i^{\text{sa}} \, dS; \quad (39a)$$

$$\int_{\bar{\Gamma}_s} \bar{\sigma}_{ij}^{(0)} \frac{\partial \bar{\eta}_i^{\text{st}}}{\partial \bar{z}_j} \frac{\partial \bar{u}_s^{(0)}}{\partial \bar{x}_t} \, d\bar{\mathbf{z}} = \frac{\partial \bar{u}_s^{(0)}}{\partial \bar{x}_t} \int_{\partial \bar{\Gamma}_m} \bar{\sigma}_{ij}^{(0)} m_j \bar{\eta}_i^{\text{st}} \, dS, \quad (39b)$$

where the fixed displacement BCs on the exterior boundary section $\partial \bar{\Gamma}_e$ has been used.

As a corollary, the leading-order (non-dimensional) energy stored in the BL region of an MSC is given by

$$\bar{U}_{\text{b}} \approx \frac{\delta}{2} \left(\int_{\partial \bar{\Omega}_d} \bar{\mathbb{C}}_{iakl}^{\text{H}} \frac{\partial \bar{u}_i^{(0)}}{\partial \bar{x}_\alpha} \frac{\partial \bar{u}_k^{(0)}}{\partial \bar{x}_l} \, dS_{\bar{\mathbf{x}}} + \int_{\partial \bar{\Omega}_d} \int_{\partial \bar{\Gamma}_m} \bar{\sigma}_{ij}^{(0)} m_j \bar{\xi}_i^{\text{sa}} \frac{\partial \bar{u}_s^{(0)}}{\partial \bar{x}_\alpha} \, dS \, dS_{\bar{\mathbf{x}}} + \int_{\partial \bar{\Omega}_d} \int_{\partial \bar{\Gamma}_m} \bar{\sigma}_{ij}^{(0)} m_j \bar{\eta}_i^{\text{st}} \frac{\partial \bar{u}_s^{(0)}}{\partial \bar{x}_t} \, dS \, dS_{\bar{\mathbf{x}}} \right). \quad (40)$$

Therefore, the total non-dimensional elastic energy stored in an MSC can roughly be evaluated by the sum of \bar{U}_{in} and \bar{U}_{b} . Nonetheless, evaluating these two energy portions involves the specification of the BL region $\bar{\Omega}$, which may cause ambiguities. For improvement, one may introduce a (non-dimensional) bulk energy quantity which is obtained by naturally extending the interior energy density form right to the domain boundary, that is,

$$\bar{U}_{\text{bulk}} = \frac{1}{2} \int_{\bar{\Omega}} \bar{\mathbb{C}}_{ijkl}^{\text{H}} \frac{\partial \bar{u}_i^{\text{H}}}{\partial \bar{x}_j} \frac{\partial \bar{u}_k^{\text{H}}}{\partial \bar{x}_l} \, d\bar{\mathbf{x}}. \quad (41)$$

Here \bar{U}_{bulk} differs from \bar{U}_{in} by

$$\bar{U}_{\text{bulk}} - \bar{U}_{\text{in}} = \frac{1}{2} \int_{\bar{\Omega}} \bar{\mathbb{C}}_{ijkl}^{\text{H}} \frac{\partial \bar{u}_i^{\text{H}}}{\partial \bar{x}_j} \frac{\partial \bar{u}_k^{\text{H}}}{\partial \bar{x}_l} \, d\bar{\mathbf{x}} = \frac{\delta}{2} \int_{\partial \bar{\Omega}_d} \bar{\mathbb{C}}_{ijkl}^{\text{H}} \frac{\partial \bar{u}_i^{\text{H}}}{\partial \bar{x}_j} \frac{\partial \bar{u}_k^{\text{H}}}{\partial \bar{x}_l} \, dS_{\bar{\mathbf{x}}}, \quad (42)$$

where Equation (34) has been adopted to derive the second identity of Equation (42).

With \bar{U}_{bulk} defined by Equation (41), the residual amount of (non-dimensional) elastic energy is given by a quantity \bar{U}_{surf} purely defined over the domain boundary $\partial \bar{\Omega}$, that is,

$$\bar{U}_{\text{surf}} = \bar{U}_{\text{b}} - \frac{\delta}{2} \int_{\partial \bar{\Omega}_d} \bar{\mathbb{C}}_{ijkl}^{\text{H}} \frac{\partial \bar{u}_i^{\text{H}}}{\partial \bar{x}_j} \frac{\partial \bar{u}_k^{\text{H}}}{\partial \bar{x}_l} \, dS_{\bar{\mathbf{x}}}. \quad (43)$$

Combining the expression for \bar{U}_{b} (Equation 40) with Equation (43), we have

$$\bar{U}_{\text{surf}} = \frac{\delta}{2} \left[\int_{\partial \bar{\Omega}_d} \left(\bar{\mathbb{C}}_{iakl}^{\text{H}} - \bar{\mathbb{C}}_{iakl}^{\text{H}} \right) \frac{\partial \bar{u}_i^{\text{H}}}{\partial \bar{x}_\alpha} \frac{\partial \bar{u}_k^{\text{H}}}{\partial \bar{x}_l} \, dS_{\bar{\mathbf{x}}} - \int_{\partial \bar{\Omega}_d} \bar{\mathbb{C}}_{iNkl}^{\text{H}} \frac{\partial \bar{u}_i^{\text{H}}}{\partial \bar{x}_N} \frac{\partial \bar{u}_k^{\text{H}}}{\partial \bar{x}_l} \, dS_{\bar{\mathbf{x}}} + \int_{\partial \bar{\Omega}_d} \int_{\partial \bar{\Gamma}_m} \bar{\sigma}_{ij}^{(0)} m_j \bar{u}_i^{(1)} \, dS \, dS_{\bar{\mathbf{x}}} \right]. \quad (44)$$

Several issues are worth being mentioned with regard to the energy quantities introduced above.

Firstly, the energy formulation derived here is linked with the force equilibrium equations given in Section 2.3. To be precise, the minimisation of $\overline{\mathcal{U}}_{\text{bulk}} + \overline{\mathcal{U}}_{\text{surf}}$ less the non-dimensional work done to the system should lead to the surface balance equation (31).

Secondly, for elliptic Dirichlet problems, the effect introduced by the BL decays exponentially as the variable perpendicular to the boundary increases.³¹ Thus for an MSC, the thickness of the BL (d), which is taken to be similar as the cell size, is a small quantity compared with the overall domain size (L), that is, $\delta = d/L \rightarrow 0$. This means

$$\lim_{\delta \rightarrow 0} \overline{\mathcal{U}}_{\text{surf}} / \overline{\mathcal{U}}_{\text{bulk}} = 0. \quad (45)$$

Here for simplicity, the contribution from the surface energy is neglected for modelling the BL effect.

2.5 | Re-dimensionalisation

To facilitate subsequent computation, we now summarise the key formulation derived above in a dimensional sense. This is normally done by simply removing the symbol “-” in the original non-dimensional formulation. Here for simplicity, we ignore the energy contribution from the BL of an MSC, but only consider the BL effect on the actual stress distribution. To this end, one simply solves for the homogenised stress field σ_{ij}^H (and the homogenised displacement field u_i^H) in the same way as the traditional AH approach. Once the homogenised problem is solved, the actual fine-scale stress distribution with an interior cell and a BL cell, based on Equations (11b) and (24), can be approximated by

$$\sigma_{ij} \approx \left(\mathbb{C}_{ijkl} + \mathbb{C}_{ijst} \frac{\partial \xi_s^{kl}}{\partial \bar{z}_t} \right) \frac{\partial u_k^H}{\partial x_l}; \quad (46a)$$

$$\tilde{\sigma}_{ij} \approx \left(\mathbb{C}_{ijk\alpha} + \mathbb{C}_{ijst} \frac{\partial \xi_s^{k\alpha}}{\partial \bar{z}_t} \right) \frac{\partial u_k^H}{\partial x_\alpha} + \mathbb{C}_{ijst} \frac{\partial \tilde{\eta}_s^{kl}}{\partial \bar{z}_t} \frac{\partial u_k^H}{\partial x_l}. \quad (46b)$$

3 | BOUNDARY LAYER FORMULATION IN MORE GENERALISED SITUATIONS

In the previous section, the discussion is limited to the situation of spatially periodic MSC subject to displacement BCs. However, in this section, BL formulation in more generalised scenarios will be considered. Our investigations will be extended for SVMSC and/or for traction BCs. Throughout the section, emphasis will be drawn over the issue on how the generalised situations differ from the reference case that is examined in detail in Section 2.

3.1 | Situation with applied traction

Generalisation over the displacement type of imposed BC is firstly studied. To this end, we here consider the BC with an applied traction field \mathbf{t}^0 on $\partial\Omega_t$, that is,

$$\mathbb{C}_{ijkl} \frac{\partial u_k}{\partial x_l^\epsilon} n_j \Big|_{\partial\Omega_t} = t_i^0, \quad \text{for } i = 1, \dots, N. \quad (47)$$

Such a change in BC should lead to hierarchic modifications as follows.

At $\mathcal{O}(1/\epsilon^2)$, the BC on the outer boundary in problem (16) should be changed to be $\overline{\mathbb{C}}_{ijkl} \frac{\partial \bar{u}_k^{(0)}}{\partial \bar{z}_l} m_j \Big|_{\partial\tilde{\Upsilon}_\epsilon} = 0$, but this does not affect the conclusions originally drawn at this order. The leading-order BL displacement field is still found independent of the microscopic coordinates $\bar{\mathbf{z}}$, and the natural extension in the interior displacement field up to the structural boundary, that is, Equation (18) still holds.

At $\mathcal{O}(1/\epsilon)$, traction BCs are expected on the outer cell boundary $\partial\tilde{\Upsilon}_\epsilon$. Now as the external loads are imposed both on $\partial\tilde{\Upsilon}_\epsilon$ and matching boundary $\partial\tilde{\Upsilon}_m$, there is an issue on solution existence, that is, the traction BCs must be declared, such

that the total traction applied to the BL cell vanishes. When the change in BC for the cell problem related to variable $\tilde{\xi}$, corresponding to problem (21), is considered, Equation (21e) becomes

$$\tilde{\xi}_k^{\beta} \Big|_{\partial\tilde{Y}_e} = 0 \Rightarrow \left(\bar{\mathbb{C}}_{ijk\alpha} \delta_{ks} \delta_{\alpha\beta} + \bar{\mathbb{C}}_{ijkl} \frac{\partial \tilde{\xi}_k^{\beta}}{\partial \tilde{z}_l} \right) m_j \Big|_{\partial\tilde{Y}_e} = 0. \quad (48)$$

But to modify the BC in cell problem (22) for variable $\tilde{\eta}$, extra treatments are needed. Given that the (non-dimensional) traction $\tilde{\mathbf{t}}^0$ are a macroscopically defined field, the corresponding components can be roughly treated uniform on $\partial\tilde{Y}_e$ in the BL cell. The overall balance condition thus reads

$$\tilde{t}_i^0 = \frac{1}{|\partial\tilde{Y}_e|} \int_{\partial\tilde{Y}_m} \bar{\sigma}_{ij}^{(0)} m_j \, d\Gamma = \Sigma_{ikl}^{(0)} \frac{\partial \tilde{u}_k^{(0)}}{\partial \tilde{x}_l}, \quad (49)$$

where

$$\Sigma_{ikl}^{(0)} = \frac{1}{|\partial\tilde{Y}_e|} \int_{\partial\tilde{Y}_m} \left(\bar{\mathbb{C}}_{ijkl} + \bar{\mathbb{C}}_{ijst} \frac{\partial \tilde{\xi}_s^{kl}}{\partial \tilde{z}_t} \right) m_j \, d\Gamma, \quad (50)$$

are the effective and microscopically uniform traction components so as to meet the overall balance requirement.

Thus the cell problem for variable $\tilde{\eta}$ can be established if one swaps Equation (22e) by

$$\tilde{\eta}_k^{st} \Big|_{\partial\tilde{Y}_e} = 0 \Rightarrow \bar{\mathbb{C}}_{ijkl} \frac{\partial \tilde{\eta}_k^{st}}{\partial \tilde{z}_l} m_j \Big|_{\partial\tilde{Y}_e} = \Sigma_{ist}^{(0)}, \quad (51)$$

and the solution existence of the resulting cell problem can be ensured simultaneously.

At $\mathcal{O}(1)$, the change in the type of imposed BC should not affect the form of the homogenisation formula, although the effective BL formulation is different because of the change in $\tilde{\xi}$ and $\tilde{\eta}$ by Equations (48) and (51).

3.2 | Spatially varying microstructures

In practical, microstructure may be filled in a region bearing irregular shape, and the infilling microstructure may have to be gradually varying in space then, as the one shown in the right panel of Figure 3.

3.2.1 | Geometric representation and spatial transformation

As discussed by Zhu et al.,¹⁸ the essence in the representation of an SVMSC is to introduce a macroscopically smooth mapping function, say, $\mathbf{y} = \mathbf{y}(\mathbf{x})$, such that the configuration becomes periodic when measured in $\bar{\mathbf{y}}$ coordinates, as shown in Figure 3.

In theory, the choice for this mapping function is rather arbitrary. But restrictions are normally required for more practical usage. For instance, maintaining the completeness in cell geometry at multi-scale boundaries seems quite critical for the whole structure serving as qualified tuning devices of acoustic wave. Nonetheless, for a given domain in which microstructure will be infilled in, it is not an easy task to ensure such cell completeness at the boundary. To this end, the mapping function here is specified to be the B-spline function, because they are often employed to determine the profile of a component digitalised from the computer aided design platform.

In contrast with the mapping operation adopted by Zhu et al.,¹⁸ we here consider using B-spline function to map a periodic structure to an SVMSC, which is effectively $\mathbf{x} = \mathbf{y}^{-1}(\mathbf{y})$ with reference to Figure 3. Suppose such a mapping function is given by $\mathbf{x} = \mathbf{S}(\mathbf{y})$. Then the specific expression of B-spline function reads

$$\mathbf{S}(\mathbf{y}^1, \mathbf{y}^2) = \sum_{i=0}^{n-1} \sum_{j=0}^{m-1} N_{i,p}(\mathbf{y}^1) N_{j,q}(\mathbf{y}^2) \mathbf{P}_{ij}, \quad (52)$$

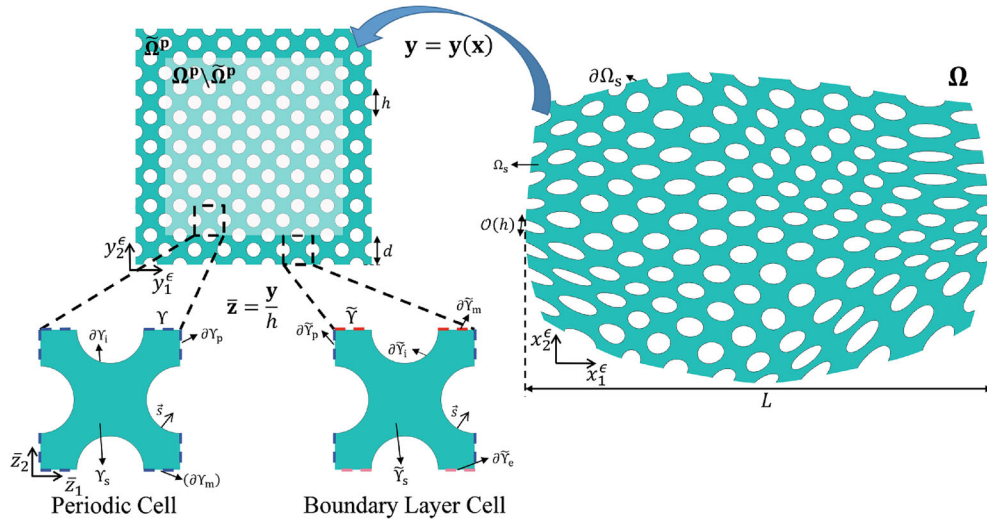


FIGURE 3 Representation of an multi-scale configuration decorated with gradually varying microstructure (right panel), which can be generated by space distortion enabled with a macroscopically smooth mapping function $\mathbf{y} = \mathbf{y}(\mathbf{x})$.

where $\mathbf{P}_{i,j} = (x_{ij}^1, x_{ij}^2) \in \mathbb{R}^2$ represent the coordinates of the $n \times m$ control points, $N_{i,p}(y^1)$ and $N_{j,q}(y^2)$ are the B-spline basis functions (piecewise polynomials) of degree p and q , which are determined by the knot vectors $U_{1 \times (n+p+1)}$ and $V_{1 \times (m+q+1)}$, respectively. One can refer to Appendix B for greater details associated with B-spline and the parameters adopted.

Among many properties of B-spline functions,³⁹ the most intuitive benefit of adopting B-spline is its capability accommodating local adjustment. As the position of control points $\mathbf{P}_{i,j}$ gets changed, only the function values of $\mathbf{S}(\mathbf{y})$ within the region $(y^1, y^2) \in [y_i^1, y_{i+p+1}^1] \times [y_j^2, y_{j+q+1}^2]$ is affected, which enables us to freely change the geometry of the model as well as the geometry of microstructure inside, by simply moving the control points. Besides, as long as the periodic structure bears complete cells in the BL, as shown in Figure 3, the cell completeness in the resulting SVMSC with the use of B-spline mapping is automatically guaranteed.

With the linkage between an SVMSC and a periodic structure established, the AH formulation is then enabled for the interior of the configuration.¹⁸

Here the spatially variance is taken into account by means of the spatial gradient of the mapping function, i.e.,

$$\mathbf{J}_{ij} = \frac{\partial y_i}{\partial x_j}, \quad \text{for } i, j = 1, \dots, N. \quad (53)$$

Upon spatial transformation, locally periodic oscillation can be assured w.r.t. the coordinates measured in $\bar{\mathbf{y}}$. Therefore, for an SVMSC, the (non-dimensional) local coordinates should be defined by

$$\bar{\mathbf{z}} = \frac{\mathbf{y}(\mathbf{x})}{h}, \quad (54)$$

where h is recalled to be a parameter characterising the length of the microscopic cell, and scale separation here is then introduced by

$$\frac{\partial}{\partial \bar{x}_i^\epsilon} = \frac{\partial}{\partial x_i} + \frac{J_{ki}}{\epsilon} \frac{\partial}{\partial \bar{z}_k}, \quad (55)$$

in the interior domain. For greater details about the asymptotic expansions of quantities in the SVMSC interior, one may refer to Reference 18.

Such a rule for scale separation can be extended to the BL formulation. Here a natural coordinate system attached to the BL of an SVMSC is constructed, that is, at each BL section, we always let $x_N = 0$. Hence, we have $\partial \bar{y}_\alpha / \partial \bar{x}_N = 0$, $\partial \bar{y}_N / \partial \bar{x}_N = 1$. Thus the last component of $\bar{\mathbf{z}}$, that is, \bar{z}_N , stays perpendicular to the boundary of the referenced periodic configuration, such as the one on the left side of Figure 3. This is equivalent to say that \bar{x}_N is along the direction perpendicular to the actual domain boundary.

TABLE 2 Multi-scale assumptions (after non-dimensionalisation) of the interior and the boundary layer (BL) regions of configurations infilled with spatially varying microstructure.

| | Interior region | Boundary layer region |
|------------|---|--|
| Rescale | $\bar{\mathbf{z}} = \bar{\mathbf{y}}/\epsilon$ | $\bar{\mathbf{z}} = \bar{\mathbf{y}}/\epsilon$ |
| Free | $\bar{x}_i \in \bar{\Omega} \setminus \bar{\Omega}, \bar{z}_i \in \Upsilon_s$ | $\bar{x}_\alpha \in \bar{\Omega}, \bar{z}_i \in \tilde{\Upsilon}_s$ |
| Variables | $i = 1, \dots, N$ | $\alpha = 1, \dots, N-1; i = 1, \dots, N$ |
| Scale | $\frac{\partial}{\partial \bar{x}_i} = \frac{\partial}{\partial \bar{x}_i} + \frac{J_{ki}}{\epsilon} \frac{\partial}{\partial \bar{z}_k}$ | $\frac{\partial}{\partial \bar{x}_\alpha} = \frac{\partial}{\partial \bar{x}_\alpha} + \frac{J_{k\alpha}}{\epsilon} \frac{\partial}{\partial \bar{z}_k}$ |
| Separation | | $\frac{\partial}{\partial \bar{x}_N} = \frac{J_{kN}}{\epsilon} \frac{\partial}{\partial \bar{z}_k}$ |

To this end, we introduce in association with the BL the same local coordinates as Equation (54), and scale separation in the BL region is carried out by

$$\frac{\partial}{\partial \bar{x}_\alpha} = \frac{\partial}{\partial \bar{x}_\alpha} + \frac{J_{k\alpha}}{\epsilon} \frac{\partial}{\partial \bar{z}_k}; \quad \frac{\partial}{\partial \bar{x}_N} = \frac{J_{kN}}{\epsilon} \frac{\partial}{\partial \bar{z}_k}. \quad (56)$$

In Table 2, the scale-separation operations are summarised within both the SVMSC interior and the BL in a comparative manner.

3.2.2 | BL formulation

Upon scale separation, the AH formulation can be derived against the SVMSC. In parallel with the derivation in Section 2.3.2, we first give a pair of BL cell problems for variables $\tilde{\xi}$ and $\tilde{\eta}$, that is,

$$\left\{ \begin{array}{l} J_{mj} \frac{\partial}{\partial \bar{z}_m} \left(\bar{\mathbb{C}}_{ijk\alpha} \delta_{ks} \delta_{\alpha\beta} + \bar{\mathbb{C}}_{ijkl} J_{rl} \frac{\partial \tilde{\xi}_k^{s\beta}}{\partial \bar{z}_r} \right) = 0, \text{ in } \tilde{\Upsilon}_s; \end{array} \right. \quad (57a)$$

$$\left(\bar{\mathbb{C}}_{ijk\alpha} \delta_{ks} \delta_{\alpha\beta} + \bar{\mathbb{C}}_{ijkl} J_{rl} \frac{\partial \tilde{\xi}_k^{s\beta}}{\partial \bar{z}_r} \right) J_{mj} S_m \Big|_{\partial \tilde{\Upsilon}_i} = 0; \quad (57b)$$

$$\left\{ \begin{array}{l} \tilde{\xi}_i^{s\beta}, \frac{\partial \tilde{\xi}_i^{s\beta}}{\partial \bar{z}_j} \text{ periodic on } \partial \tilde{\Upsilon}_p; \end{array} \right. \quad (57c)$$

$$\left(\bar{\mathbb{C}}_{ijk\alpha} \delta_{ks} \delta_{\alpha\beta} + \bar{\mathbb{C}}_{ijkl} J_{rl} \frac{\partial \tilde{\xi}_k^{s\beta}}{\partial \bar{z}_r} \right) J_{mj} S_m \Big|_{\partial \tilde{\Upsilon}_m} = 0; \quad (57d)$$

$$\left\{ \begin{array}{l} \tilde{\xi}_i^{s\beta} \Big|_{\partial \tilde{\Upsilon}_e} = 0, \end{array} \right. \quad (57e)$$

and

$$\left\{ \begin{array}{l} J_{mj} \frac{\partial}{\partial \bar{z}_m} \left(\bar{\mathbb{C}}_{ijkl} J_{rl} \frac{\partial \tilde{\eta}_k^{st}}{\partial \bar{z}_r} \right) = 0, \text{ in } \tilde{\Upsilon}_s; \end{array} \right. \quad (58a)$$

$$\bar{\mathbb{C}}_{ijkl} J_{rl} \frac{\partial \tilde{\eta}_k^{st}}{\partial \bar{z}_r} J_{mj} S_m \Big|_{\partial \tilde{\Upsilon}_i} = 0; \quad (58b)$$

$$\left\{ \begin{array}{l} \tilde{\eta}_i^{st}, \frac{\partial \tilde{\eta}_i^{st}}{\partial \bar{z}_j} \text{ periodic on } \partial \tilde{\Upsilon}_p; \end{array} \right. \quad (58c)$$

$$\bar{\mathbb{C}}_{ijkl} J_{rl} \frac{\partial \tilde{\eta}_k^{st}}{\partial \bar{z}_r} m_j \Big|_{\partial \tilde{\Upsilon}_m} = \left(\bar{\mathbb{C}}_{ijst} + \bar{\mathbb{C}}_{ijkl} J_{rl} \frac{\partial \xi_k^{st}}{\partial \bar{z}_r} \right) J_{mj} S_m \Big|_{\partial \tilde{\Upsilon}_m}; \quad (58d)$$

$$\left\{ \begin{array}{l} \tilde{\eta}_i^{st} \Big|_{\partial \tilde{\Upsilon}_e} = 0, \end{array} \right. \quad (58e)$$

where \mathbf{s} is the outer normal at a boundary point of the cell after mapping, and the Dirichlet BCs are imposed at the SVMSC boundary for the moment.

With the two variables $\tilde{\xi}$ and $\tilde{\eta}$ fully determined, the fine-scale stress field of the BL can be resolved by

$$\tilde{\sigma}_{ij}^{(0)} = \left(\mathbb{C}_{ijk\alpha} + \mathbb{C}_{ijst} J_{rt} \frac{\partial \tilde{\xi}_s^{k\alpha}}{\partial \tilde{z}_r} \right) \frac{\partial u_k^{(0)}}{\partial x_\alpha} + \mathbb{C}_{ijst} J_{rt} \frac{\partial \tilde{\eta}_s^{kl}}{\partial \tilde{z}_r} \frac{\partial u_k^{(0)}}{\partial x_l}. \quad (59)$$

If the SVMSC is applied with an external load \mathbf{t}^{-0} at the boundary, the original displacement BCs in the BL cell problems (57) and (58) should be swapped by

$$\left(\bar{\mathbb{C}}_{ijk\alpha} \delta_{ks} \delta_{\alpha\beta} + \bar{\mathbb{C}}_{ijkl} J_{rt} \frac{\partial \tilde{\xi}_k^{s\beta}}{\partial \tilde{z}_r} \right) J_{mj} s_m \Big|_{\partial \tilde{Y}_e} = 0, \quad (60)$$

and

$$\bar{\mathbb{C}}_{ijkl} J_{rt} \frac{\partial \tilde{\eta}_k^{st}}{\partial \tilde{z}_r} J_{mj} s_m \Big|_{\partial \tilde{Y}_e} = \Sigma_{ist}^{(0)}, \quad (61)$$

respectively. Here the microscopically uniform traction components $\Sigma_{ist}^{(0)}$ take the same definition as implied by Equation (50).

3.3 | Situations with different boundary orientations

The derivation above limits itself in situation where the overall boundary section of interest stays coincident with the plane $\partial \bar{\Omega} = \{\bar{\mathbf{x}} | \bar{x}_N = 0\}$. When boundary sections bearing a different orientation, generalisation from the present results is necessary.

The key idea is to transform the BL solutions intended for the boundary $x_N = 0$ in accordance with the boundary of interest. For example, the solutions for two types of BL cell problems on a certain boundary are assumed to be $\tilde{\xi}_i^{j\alpha}$, $\tilde{\eta}_i^{jk}$, then for BL cells composed of isotropic base materials, their solutions can be associated with the original ones (with a symbol ' \wedge ') through the following formula

$$\tilde{\xi}_i^{j\alpha} = Q_{ik} Q_{js} Q_{\alpha\beta} \tilde{\xi}_k^{s\beta}; \quad (62a)$$

$$\tilde{\eta}_i^{jk} = Q_{ir} Q_{js} Q_{kt} \tilde{\eta}_r^{st}, \quad (62b)$$

where \mathbf{Q} is a certain orthogonal matrix, and the relevant proof is available in Appendix A.

4 | COMPUTATIONAL FEASIBILITY ENABLED BY ML

With the asymptotic expressions provided, we now consider using surrogate models (referring exclusively to the neural networks, or abbreviated as NNs) for predicting the local maximum von Mises stress (LMvMS) at each point near the boundary on this basis. Note that the relationship between the equivalent elasticity tensor in the SVMSC interior and the corresponding cell geometry should be superseded by a surrogate model likewise. But since the issue has been elaborated in the work of Ma et al.,⁴⁰ we are mainly focused on adopting the NNs to represent related solutions for the BL cell problem.

4.1 | Localisation

Localised properties, such as strength, always see their priorities of engineering concerns which reflects the widespread demand for the efficient prediction of the stress and location of local failure in such multi-scale structures. However,

performing localisation operation on the basis of homogenisation results usually suffers from methodological paradox. Homogenisation tends to return mean-field results, while material strength highly depends on the local geometric details. Besides being different from the interior of an MSC, the BL region is often more susceptible to failure initiation. Here we investigate the localisation formulation for the prediction of the LMvMSes near the boundary of an MSC.

As from the AH results, zero-order stress tensors $\tilde{\sigma}_{ij}^{(0)}$ inside the BL region are obtained (Equations 46b and 59), whose corresponding eigenvalue problems yield the principal stresses: $\tilde{\sigma}_I^{(0)} > \tilde{\sigma}_{II}^{(0)} > \tilde{\sigma}_{III}^{(0)}$ (from large to small). Then the von Mises stress of a particular point in the cell can be calculated by

$$\tilde{\sigma}_{vM}^{(0)} = \sqrt{\frac{\left(\tilde{\sigma}_I^{(0)} - \tilde{\sigma}_{II}^{(0)}\right)^2 + \left(\tilde{\sigma}_{II}^{(0)} - \tilde{\sigma}_{III}^{(0)}\right)^2 + \left(\tilde{\sigma}_{III}^{(0)} - \tilde{\sigma}_I^{(0)}\right)^2}{2}}. \quad (63)$$

Suppose the configuration is made of materials which can withstand a maximum equivalent stress of σ_{\max}^* . Thus for safety assessment, the inequality

$$\max\left(\left[\sigma_{vM}^{(0)}\right], \left[\tilde{\sigma}_{vM}^{(0)}\right]\right) \leq \sigma_{\max}^*, \quad (64)$$

should be verified for all $\mathbf{x} \in \Omega, \bar{\mathbf{z}} \in \Upsilon_s \cup \tilde{\Upsilon}_s$, where $\sigma_{vM}^{(0)}$ is the LMvMS calculated from a point in the domain interior.²⁷ The symbol “[•]” here denotes the set of von Mises stresses corresponding to all points investigated.

Solution to the cell problems of periodic structures is independent of the macroscopic position a cell lies, so the elasticity tensor of all global points can be represented by the \mathbb{C}_{ijkl}^H of one single periodic cell. According to the expressions of stresses presented in Equations (46a) and (46b), the local stress in a representative cell is directly obtained by the product of solutions to a set of determinate cell problems and homogenised displacement gradient at the macro point of interest. Thus, the calculation of local stresses in the periodic case is something straightforward, and a follow-up discussion will focus on localisation scheme for the case of spatially varying microstructures.

For graded microstructures, the evaluation of stress fields $\sigma^{(0)}$ and $\tilde{\sigma}^{(0)}$ calls for results of the interior cell and the BL cell, respectively, which is computationally expensive due to the dependence of cell problems to be solved on macroscopic coordinate the cell locates in. Thereby, in order to check the strength, one has to traverse the von Mises stresses at all possible macro points and substitute them into Equation (64) for verification, during which cell problems in both regions will be solved repeatedly and extensively, leading to a significant decrease in efficiency. To this end, ML comes to the rescue.

Under the scale separation framework, each cell represented by Υ or $\tilde{\Upsilon}$ is assumed to be attached to a macro point, in the vicinity of which we can accordingly define the LMvMS, that is,

$$\sigma_{\max}(\mathbf{x}) = \begin{cases} \max\left(\sigma_{vM}^{(0)}\right), & \bar{\mathbf{z}} \in \Upsilon_s; \\ \max\left(\tilde{\sigma}_{vM}^{(0)}\right), & \bar{\mathbf{z}} \in \tilde{\Upsilon}_s, \end{cases} \quad (65)$$

such that σ_{\max} is only a function of the macroscopic variable, which characterises the maximum von Mises stress around point \mathbf{x} .

Next, we aim to identify the conceptual definition given in the above equation as a function relation of factors affecting the distribution of localised stress fields. Two factors are intuitive from Equation (59), that is the homogenised displacement gradient $\partial \mathbf{u}^H / \partial \mathbf{x}$ and Jacobian components J_{ij} . Besides, the determination of cell problems requires specifying the corresponding geometric domains, whose information is completely stored in cell topology description function (TDF) Φ . Finally, a definite but implicit relationship linking σ_{\max} and multiple factors is identified, that is,

$$\sigma_{\max} = F\left(\epsilon^H; \mathbf{J}, \Phi\right), \quad (66)$$

which is expected to be represented with the NNs.

4.2 | Determination of input arguments

The NNs are expected to substitute the relation of stress-localisation (Equation 66) and relax the requirement to obtain analytical solutions from the AH. To further improve the performance of NN fitting, one should first consider reducing

the dimension of input arguments as much as possible, three major criteria are adopted here to determine the proper inputs: (a) Extraction of geometric meaning; (b) Compression of sample space⁴⁰; (c) Input rescaling.²⁷

First, extraneous variables can be eliminated with a thorough understanding of the geometric meanings of some arguments. For instance, the inverse matrix of Jacobian matrix \mathbf{J}^{-1} maps a square cell to a parallelogram, and such a process can be fully described by three parameters λ , θ_1 and θ_2 (See Figure 4), generally, the following limits are imposed on their ranges

$$\frac{1}{\lambda_{\max}} \leq \lambda \leq \lambda_{\max}, \quad 0 \leq \theta_1 < 2\pi, \quad \theta_{\min} \leq \theta_2 \leq \pi - \theta_{\min}, \quad (67)$$

to prevent distortion of cells. At the cell level, we can drop the rotation angle θ_1 because the change of elasticity tensor due to rotation is explicit. Thus only the effects of stretching and torsional deformation are considered.

Notice that there are two ways to decompose the deformation mode of a microscopic cell, that is, deformation followed by rotation or rotation followed by deformation. As demonstrated, only the first way enables \mathbb{C}_{ijkl}^H in the real space to be derived from the solution of cells ignoring the rotation angle.⁴¹ Consequently, the specific decomposition is expressed as

$$\mathbf{J}^{-1} = \begin{bmatrix} \cos \theta_1 & \lambda \cos(\theta_1 + \theta_2) \\ \sin \theta_1 & \lambda \sin(\theta_1 + \theta_2) \end{bmatrix} = \begin{bmatrix} \cos \theta_1 & -\sin \theta_1 \\ \sin \theta_1 & \cos \theta_1 \end{bmatrix} \begin{bmatrix} 1 & \lambda \cos \theta_2 \\ 0 & \lambda \sin \theta_2 \end{bmatrix} = \mathbf{Q}\mathbf{R}, \quad (68)$$

where \mathbf{Q} is an orthogonal matrix representing pure rotation and \mathbf{R} is an upper triangular matrix representing pure deformation. We ignore rigid body rotation of cell in the subsequent data set construction process, so the local Jacobian matrix will be the special case of $\mathbf{Q} = \mathbf{I}$, where \mathbf{I} is a identity matrix, denoted as $\tilde{\mathbf{J}} = \mathbf{R}^{-1}$.

For the second criterion, it is proved that σ_{\max} remains unchanged when each component of $\tilde{\mathbf{J}}$ is multiplied by the same non-zero constant, therefore we require $\det(\tilde{\mathbf{J}}) = 1$, that is, $\tilde{\mathbf{J}}'_{ij} = [\det(\tilde{\mathbf{J}})]^{-\frac{1}{N}} \tilde{\mathbf{J}}_{ij}$.

And for cases of linear elasticity, the criterion (c) allows Equation (66) to be re-expressed as

$$\sigma_{\max} = \varepsilon^* F\left(\frac{\varepsilon^H}{\varepsilon^*}; \lambda, \theta_2, \Phi\right), \quad (69)$$

here, for the interior cell, we choose $\varepsilon^* = \sqrt{(u_{11}^H)^2 + (u_{22}^H)^2 + (\gamma_{12}^H)^2}$, $\gamma_{12}^H = u_{12}^H + u_{21}^H$, while for the BL cell, $\varepsilon^* = \sqrt{(u_{11}^H)^2 + (u_{22}^H)^2 + (u_{12}^H)^2 + (u_{21}^H)^2}$, $u_{ij}^H = \partial u_i^H / \partial x_j$, for $i, j = 1, \dots, N$. The argument set regarding the homogenised displacement gradient is thus normalised, and the complexity of the corresponding network input is reduced by one dimension in a sense.

4.3 | Construction of data sets

Low discrepancy sequence is adopted to ensure the input data points form a more complete coverage of the space they span. Based on the theoretical derivation of the preceding AH process, we can naturally distil the core steps to generate

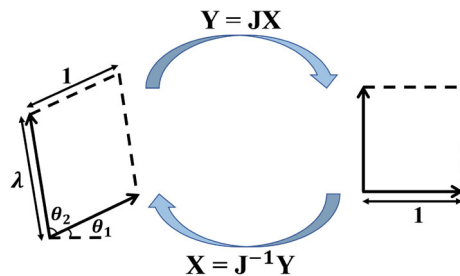


FIGURE 4 Geometric meaning behind the mapping between microscopic cells. λ measures the length relative to the other edge, θ_1 is the counterclockwise rotation angle of the cell and θ_2 is the angle between adjacent sides of a parallelogram.

TABLE 3 Detailed steps for generating a single data point for the neural networks (NNs) characterising the local maximum stresses calculated based on the solutions for the interior and the boundary layer (BL) regions, respectively.

| | |
|-----------------|---|
| Interior region | <p>Step 1. Specifying Values of Input Arguments. For an interior cell with a given TDF, specific values are assigned to λ and θ_2 within the range specified in Equation (67) to form the cell geometry Y_s, meanwhile a set of $u_{11}^H, u_{22}^H, \gamma_{12}^H$ is assigned within a certain range;</p> <p>Step 2. Solving Cell Problems. A solvable cell problem (that with periodic BCs) has been uniquely identified in the previous step, whose solution yields ξ_i^{jk}. Results at boundary ∂Y_m are extracted separately for subsequent matching conditions;</p> <p>Step 3. Computing the Local Stress Tensor in an interior cell. With the calculated u_{ij}^H and ξ_i^{jk}, the stress tensor $\sigma_{ij}^{(0)}$ at each point in cell domain are available;</p> <p>Step 4. Computing the Output Value of NN. By solving eigenvalues for each set of $\sigma_{ij}^{(0)}$, von Mises stress σ_i^{VM} is then obtained, i denotes the ith point selected in cell. When i traversing all points, $\sigma_{\max} = \max(\sigma_i^{VM})$ gives the output of the NN. Thus a data point $(u_{11}^H, u_{22}^H, \gamma_{12}^H, \lambda, \theta_2, \Phi; \sigma_{\max})$ in the input–output space of the NN summarising results of the interior problem is presented.</p> |
| Boundary layer | <p>Step 1. Specifying Values of Input Arguments. Specific values are assigned to λ and θ_2 likewise, forming the geometry of a BL cell \tilde{Y}_s, also a set of homogenised displacement gradient $u_{11}^H, u_{22}^H, u_{12}^H, u_{21}^H$ is assigned within a certain range;</p> <p>Step 2. Solving Cell Problems. Two types of cell problems (57) and (58) can be solved in domain defined in the previous step to get $\tilde{\xi}_i^{\alpha}, \tilde{\eta}_i^{jk}$. The values $\xi_i^{jk} _{\partial Y_m}$ extracted before are needed for the determination of $\tilde{\eta}_i^{jk}$;</p> <p>Step 3. Computing the Local Stress Tensor in an interior cell. Stress $\tilde{\sigma}_{ij}^{(0)}$ is available from Equation (59) based on the results obtained above;</p> <p>Step 4. Computing the Output Value of NN. Similar to the operation of the interior region, network output in this case goes like $\sigma_{\max} = \max(\tilde{\sigma}_i^{VM})$. Thus a data point $(u_{11}^H, u_{22}^H, u_{12}^H, u_{21}^H, \lambda, \theta_2, \Phi; \sigma_{\max})$ in data set of the NN summarising results of the BL problem is presented.</p> |

a data point, and the specific implementation process varies in the two regions. Such steps corresponding to the interior cell and BL cell are specified in Table 3.

Theoretically, an infinite number of data points can be generated by repeating the above steps under various values of input arguments, which is well suited for parallel computing since no correlation exists between different data points of the NN related to the interior cells; but for the NN characterising results of the BL, once solutions of the interior cell are determined, the corresponding generating processes are also independent of each other and can be carried out in parallel.

4.4 | Specification of argument values and performance of network training

In this subsection, we will present specific parameters selected in this article for the determination of cell geometry and the construction of NN. Take cell configurations shown in Figure 5 as an example.

For data generalisation, we need to assign values randomly to the two sets of controlling variables as discussed in Section 4.2. For the design variables carrying the information of the macroscopic variance, we refer to the geometrically meaningful parameters (r, λ, θ_2) shown in Figure 4 instead of the components of the original Jacobian matrix \mathbf{J} . The variable r is chosen to capture the change in the TDF Φ of the initial unit cell. Here the parameters (r, λ, θ_2) are randomly evaluated within $[0.1, 0.3] \times [1/4, 4] \times [\pi/6, 5\pi/6]$, and 300 samples are collected for them.

As for the design variables indicating the on-site homogenised quantities, the number of such variables is different between the input arguments for the NN summarising the results of the interior cell problems and those for the NN summarising the BL cell problems. Note that an interior cell problem can be parameterised by three components, that is, $(u_{11}^H, u_{22}^H, \gamma_{12}^H)$, whose (random) evaluations are all constrained in the interval $[-1, 1]$. We here collect 300 samples for these three components. But for a BL cell problem, four parameters $(u_{11}^H, u_{22}^H, u_{12}^H, u_{21}^H)$ are required, while the bounds for the evaluation stay the same as $[-1, 1]$. Thus, the number of samples must be larger, and 400 samples are considered. Therefore, we generate $300 \times 300 = 90,000$ sets of data points to train a NN to represent the results of the interior problem, and $300 \times 400 = 120,000$ sets of data points to train a NN that characterises the results related to the BL problem.

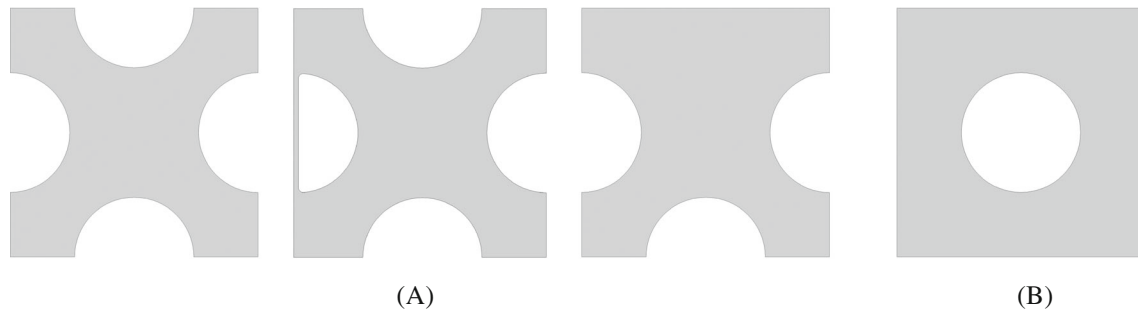


FIGURE 5 Specific configurations of the representative cells. (A) Geometric patterns of an interior cell (left), a boundary layer (BL) cell taken from the boundary section on the left side of the domain (middle) and one taken from the upper side of the domain (right). The above three types of cells constitute the interior region, displacement BL region and stress BL region of an multi-scale configuration (MSC), respectively, whose BL cells bearing a geometry different from the interior cells. The thickness of the left layer on the middle cell is 0.02 times the original length (usually taken as 1). (B) Another type of unit cell, which alone constitutes an MSC.

The training of both types of network models is implemented based on the Statistics and Machine Learning Toolbox 12.4 in MATLAB® R2022b. Levenberg–Marquardt algorithm is adopted here for the NN training models, in which the activation function is Sigmoid function and the initialisation method is Nguyen–Widrow method. We follow the general practice of arbitrarily selecting 70%, 15%, 15% of the data set as the training set, test set, and validation set for the NN, respectively. For the NN constructed based on the interior solutions, three hidden layers are adopted, with 45 neurons in the first layer and 40 neurons in the last two layers, that is, the structure of this network is (45, 40, 40); as for the NN constructed based on the BL solutions, the network structure of (55, 55, 50) is selected corresponding to the BL cell subject to displacement BCs at its outer boundary and (50, 50, 45) for that subject to stress BCs.

It is obvious to tell from the zero-order stress expressions of periodic structures that data points of both networks take the form $(u_{11}^H, u_{22}^H, \gamma_{12}^H, r)$. As explained in Section 4.1, the corresponding cell problems only need to be solved once, but we still consider employing the NN to replace such a solving-and-storing process for the sake of tremendously reducing the memory and disc footprint. In this case, $N_1 = 250, N_2 = 300$ are adopted for both data sets, and structures of the two NNs mentioned above are (30, 30, 25) and (45, 45, 35), respectively.

The performance of the trained network is measured by the root-mean-square error (RMSE). The lower the RMSE, the better the network should perform. On a graphic account, more data points get concentrated around line where the trained output equals the corresponding feeding data, such as those shown in Figure 6, and good performance from the trained neural networks is thus demonstrated.

5 | NUMERICAL EXAMPLES

Based on the previous theoretical groundwork, several numerical computations including cases of periodic and gradually-varying microstructures, BL cells subject to displacement and stress BCs, rectangular and non-rectangular domains, are implemented on the COMSOL Multi-physics® v. 5.6. platform⁴² to illustrate the impact of BL effects in different problems investigated.

For all MSCs involved hereafter, solid part materials are assumed to be elastic, isotropic and the specific values are selected as follows: the Young's modulus is fixed to $E = 200$ GPa and Poisson's ratio $\nu = 0.3$. A plane strain state is considered here to serve as the two-dimensional simplified model of the problem, and the lengths of all specimens in the third dimension is assumed to be 1 m. For simplicity, the non-dimensional BL thickness (Equation 9) is fixed at about 1 (see Reference 34 for systematic investigation of the case with square unit cells, and the case of non-square cells will be given in Section 5.1), and we will not include the surface term (Equation 44) in the minimisation of energy functional.

5.1 | Remarks on theoretical studies

The former rigorous treatment of the BL enables the exponential decay of quantities associated with the BL region in the direction perpendicular to the structure boundary,²⁸⁻³¹ which is quite inconvenient for practical implementation.

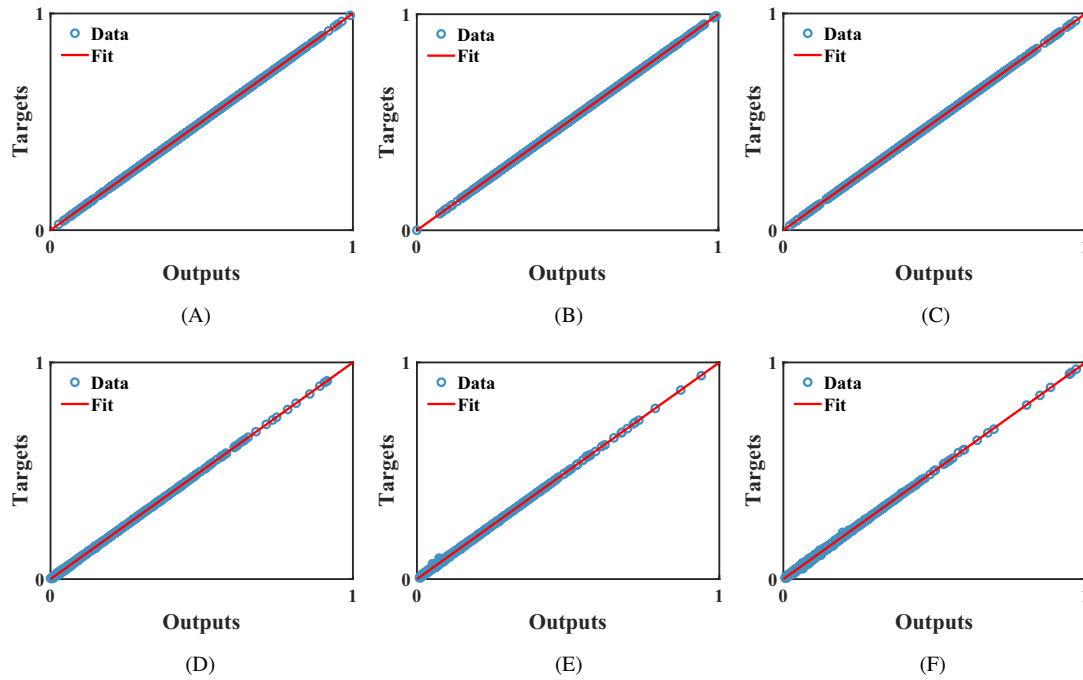


FIGURE 6 Regression graphs of the trained neural networks (NNs). (A–C) are all the cases of periodic structures, corresponding to the interior cell, boundary layer (BL) cell on a fixed edge and that on a traction-free edge, respectively; (D–F) are all under the case of spatially varying multi-scale configurations which also correspond to the same meaning as the above three, respectively. Root mean square errors of the networks training for each case are marked below the corresponding subfigure. (A) RMSE = 0.0087%; (B) RMSE = 0.012%; (C) RMSE = 0.012%; (D) RMSE = 0.12%; (E) RMSE = 0.13%; (F) RMSE = 0.24%.

Therefore, recent work has favoured an approximate way to extract the BL region separately for brute force computation,^{32,33} and this requires a pre-determination of the extent of the BL influence. Drago and Pindera have numerically demonstrated that for a periodic porous structure with square unit cell, the BL effect is confined to one layer of the constituent cell,³⁴ meaning that one period thickness suffices for the approximation of the BL behaviour.

Here, a case of a periodic porous structure with non-square constituent cell is presented to further illustrate the extent of such BL effect. We consider a periodic structure consisting of 6×5 parallelogram unit cells with a fixed left end, a given displacement $u = 0.05$ dm imposed on the right end, and the remaining two boundaries free. The cell takes a geometry similar to the left panel of Figure 4, with $\theta_1 = 0$, $\theta_2 = \pi/3$, but it is normalised to its area. In this section, the stress components recovered through traditional AH method are used to examine the accuracy of stress calculations near the boundary by comparing them with those obtained by fine-mesh FEA. From the results shown in Figure 7, it can be seen that when ϵ is not very large, the difference in each stress component is confined to a one-period thick layer near the boundary.

5.2 | The case of periodic porous structures

For configurations infilled with periodic microstructure, the geometry of BL cells can differ from that of the interior cells, and in fact any cell that smoothly connects to the interior part can be used to construct the BL region. In the discussion within this subsection, two situations will be examined: (a) the cases with geometrically identical cells where the BL cells are identical to the interior cells in shape; (b) the cases with geometrically different cells where the BL cells are different from the interior cells in shape.

5.2.1 | Cases with geometrically identical cells

We first consider a spatially periodic structure of size 7 dm \times 4 dm formed by a hollow unit cell as shown in Figure 8. This MSC is fixed to its left side, while a uniformly distributed displacement field is applied on its right side at a magnitude of $u_1 = 0.05$ dm.

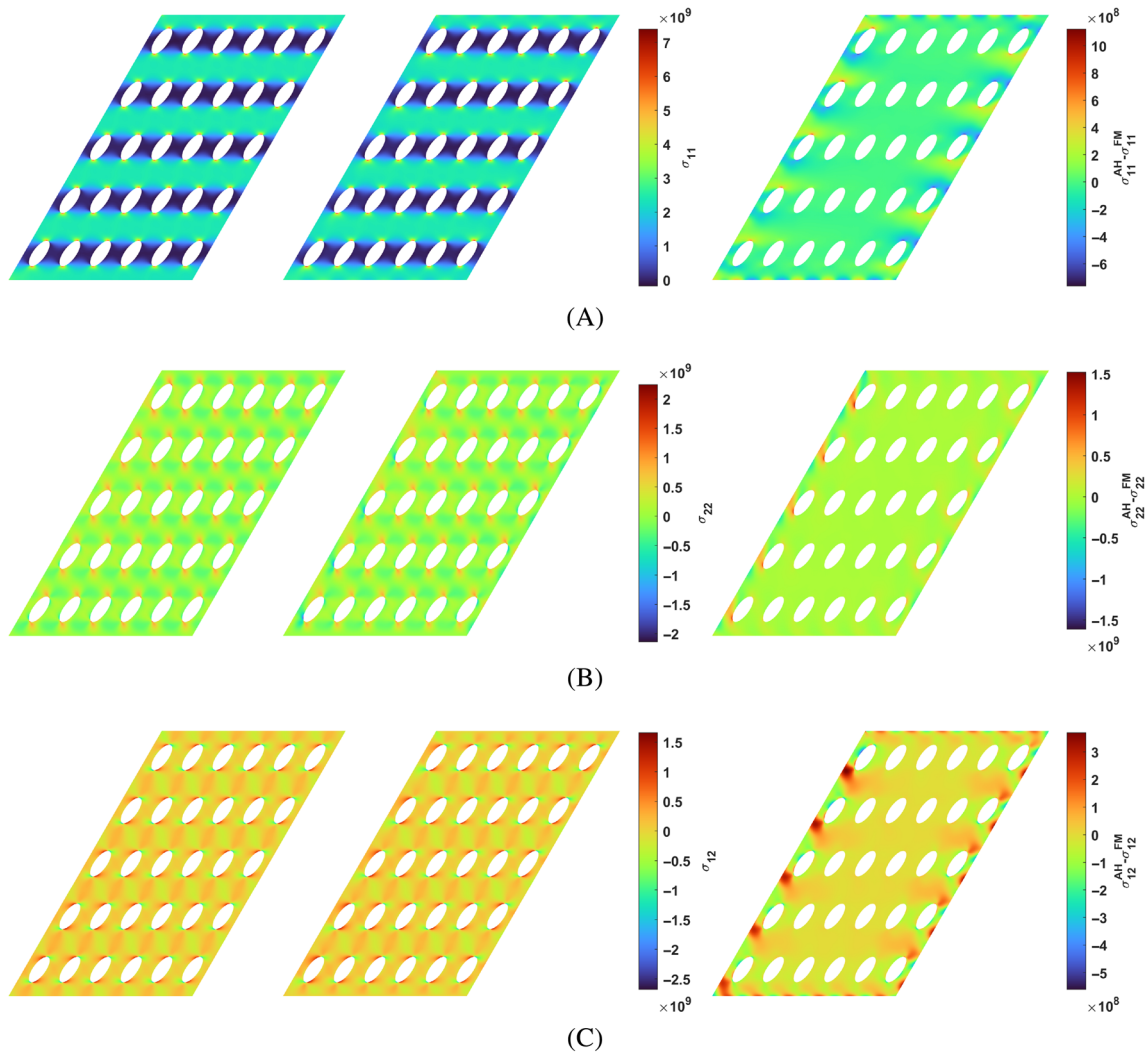


FIGURE 7 Illustration of the extent of the boundary layer (BL) effect in a periodic porous structure composed of parallelogram unit cells. The left column represents the stress components recovered through the AH method, denoted σ^{AH} ; the three figures in the middle column represent the stress components directly given by fine-mesh finite element analysis, denoted σ^{FM} ; the right column figures show the difference between the first two, that is, $\sigma^{\text{AH}} - \sigma^{\text{FM}}$. (A) Comparison of stress component σ_{11} ; (B) Comparison of stress component σ_{22} ; (C) Comparison of stress component σ_{12} .

Since the surface energy term due to the BL is neglected, the macroscopic homogenisation problem is identical to that in the AH method, particularly for periodic structures, the equivalent elasticity tensor has only to be calculated once to obtain the moduli of the whole entity. In the AH theory, solution to such a porous structure can be approximated by the combination of solutions to microscopic cell problems and macroscopic homogenisation problem, and the homogenised displacement gradients are obtained by following this traditional operation, thus determining network inputs related to the loading environment.

Now we set about investigating the reliability of two types of NNs constructed based on solutions for the interior region and the BL region, respectively, in predicting the LMvMSes near the configuration boundary, with those extracted from direct fine-mesh FEA of the MSC being served as the benchmark. The specific regions for extracting fine-scale computation results are indicated in Figure 8. Note that the “corner cells”, which are also located at the structure boundary, are not included in regions above, because they are no more periodic along any direction and have to be modelled separately for further analysis. Thus no discussion concerning “corner cells” is included for the time being.

The computation results from the present BL-homogenisation-based scheme are compared with those from fine-scale solutions, as well as those from the traditional homogenisation method (without the inclusion of BL cells). On the field boundary that lies on the left edge of the MSC, the relative deviation from the fine-scale results is found both limited,

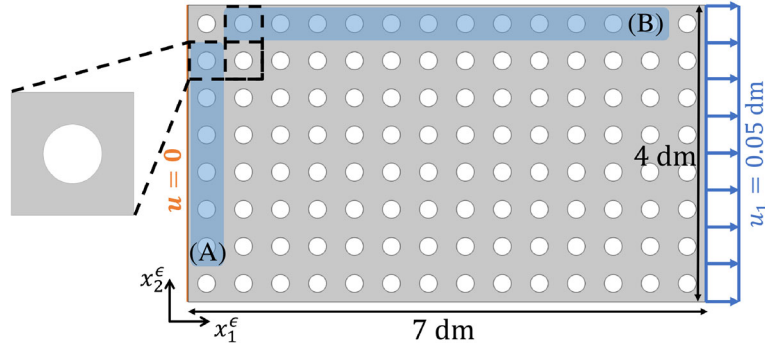


FIGURE 8 Periodic structure consists of identical unit cells taking the geometry of Figure 5B. The left boundary is fixed and a uniform displacement $u_1 = 0.05$ dm is imposed on the right end. Blue shaded areas denote regions composed of boundary layer (BL) cells subject to (A) displacement boundary conditions (BCs) $\mathbf{u} = \mathbf{0}$; (B) stress BCs $\boldsymbol{\sigma} \cdot \mathbf{n} = \mathbf{0}$, respectively, on their outer boundaries.

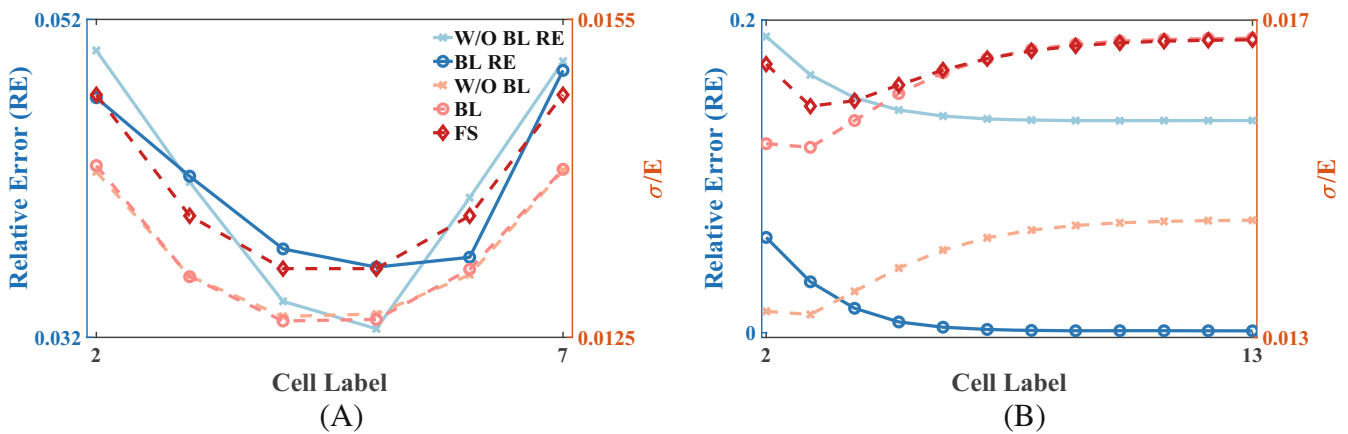


FIGURE 9 Case: Periodic microstructure with unit cells taking the geometry of Figure 5B. Comparison between values predicted by the neural networks (NNs) with the benchmark obtained from direct fine-mesh finite element analysis (FEA) of the multi-scale configuration (MSC). Two subfigures represent the examination of the LMvMSes in the blue shaded area (A) and (B) illustrated in Figure 8, respectively. Here solid lines denote quantities related to the relative errors and dashed lines denote those related to the absolute values. Explanations of abbreviations in the legend are listed. BL, boundary layer; FS, fine-scale; RE, relative error; W/O, without.

that is, $\leq 5\%$ (Figure 9A), with and without the inclusion of BL cells. But on the free edge lying on the top of the structure, as shown in Figure 9B, the use of BL formulations effectively decreases the relative error from about 19% to below 6.1%.

Note that the results presented in Figure 9 are all limited to the case the thickness of the BL (Equation 9) being the same as that of the interior cell, which is an approximate treatment. However, there is a possibility that the BL effects span multiple cell layers. We follow the previous steps to investigate the influence on final results when the BL thickness is changed to two cells. From the comparison of predictive results shown in Figure 10, the impact on the prediction accuracy caused by increasing the number of cells contained in one BL cell does not have a significant improvement over the original one, which coincides with the conclusion drawn in Section 5.1.

5.2.2 | Cases with geometrically different cells

For the second situation, we consider a configuration of size 7.02 dm \times 4 dm where the microstructure near the boundary differs from that in the interior. As shown in Figure 11, the specific configurations of constituting cells can be seen more clearly in the upper left panel. Here BCs of the structure are consistent with those described in the previous section and the thicknesses of both thin layers attached to the left and right ends are 0.01 dm.

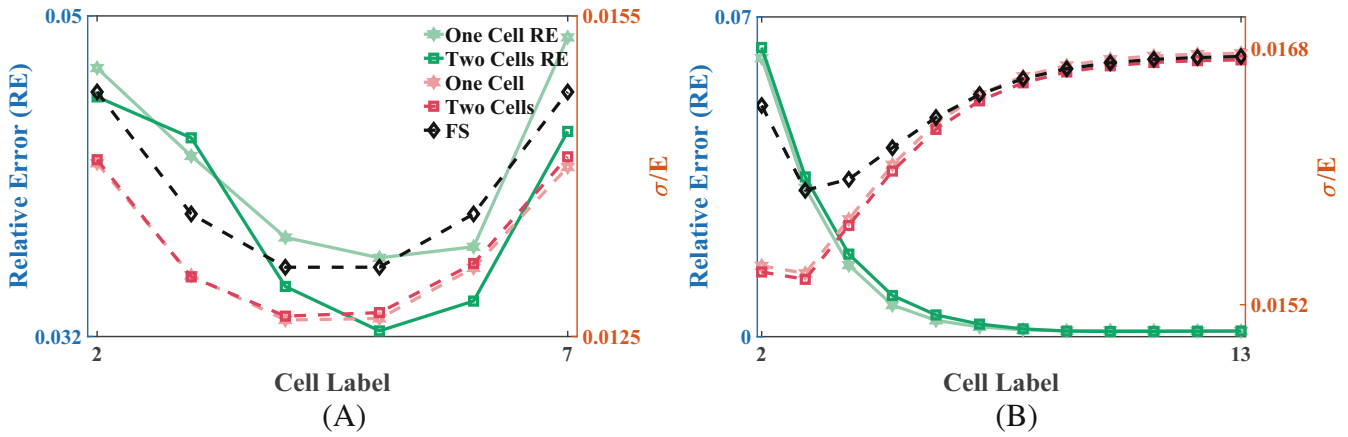


FIGURE 10 Comparison of the predictive accuracy between the neural network (NN) constructed based on boundary layer (BL) cells composed of one single unit cell and that constructed based on BL cells composed of two cells. Two subfigures correspond to results extracted from two regions (A) and (B) in Figure 8, respectively. Here solid lines denote quantities related to the relative errors and dashed lines denote those related to the absolute values. ‘One Cell’ indicates the case where the BL cell consists of one single cell. ‘Two Cells’ represents the case where the BL cell consists of two unit cells.

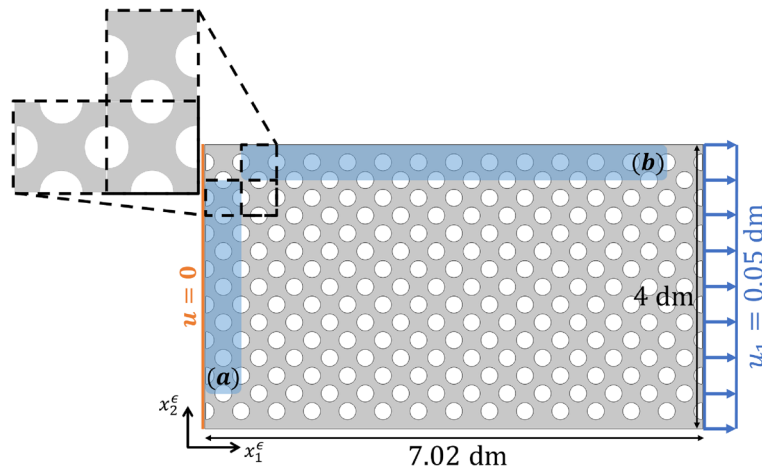


FIGURE 11 Periodic structure consists of different unit cells taking the geometry of Figure 5A. Blue shaded areas here have the same meanings as in Figure 8, and the thicknesses of both thin layers attached to the left and right ends are fixed to 0.01 dm.

Similar to Section 5.2.1, the comparison between predictions and the benchmark has also been presented in this situation in Figure 12. From which it is obvious that the predicted values given by the NN characterising the interior local maximum stress show a great deviation from fine-scale results, and the relative errors even exceed 32% when predicting the LMvMSes near the free edge of the MSC (Figure 12B), while the NN characterising the local maximum stress in the BL still maintains high accuracy.

5.3 | Cases with spatially varying structures

Unlike each macroscopic point corresponds to the identical representative cell in periodic structures, the constituent cells of an SVMSC may undergo deformation and rotation, such local behaviour are fully reflected by the Jacobian matrix (Equation 53) of the mapping function. As stated in Section 4.2, rotation angle θ_1 is neglected in the process of generating data set for the consideration of reducing the input dimension, so all values here predicted by the NNs are on the premise of $\theta_1 = 0$.

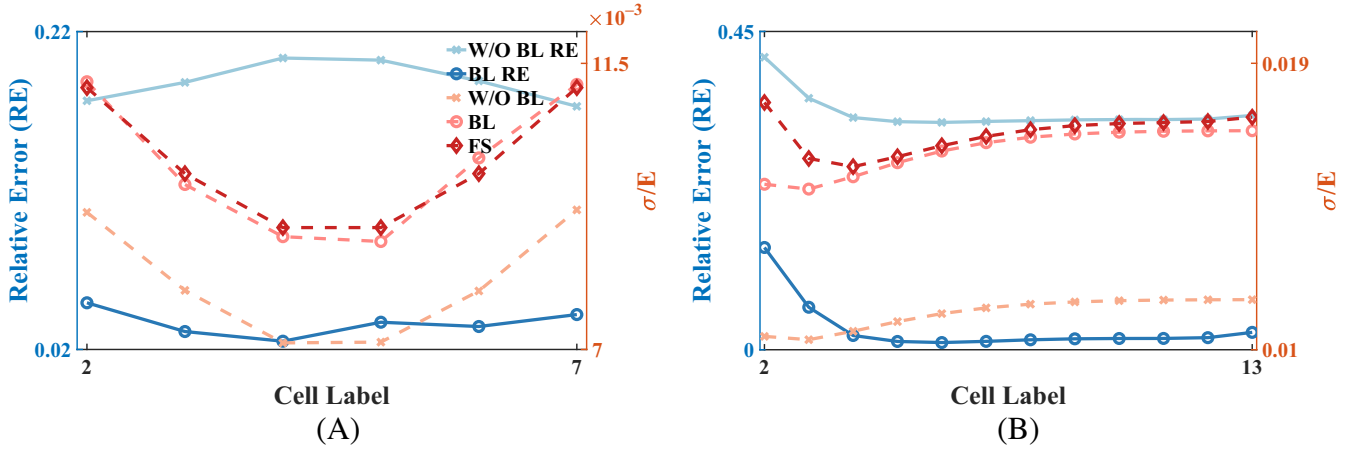


FIGURE 12 Case: Periodic microstructure with unit cells taking the geometry of Figure 5A. Two subfigures here represent the examination of the LMvMSes in the blue shaded area (A) and (B) illustrated Figure 11, respectively.

Consequently, in practical gradually varying microstructures, the input and output of the NNs should be adjusted in conjunction with the cell deformation mode, the specific approach is to apply QR factorisation (Equation 68) to the Jacobian matrix \mathbf{J} at a macroscopic point to get two matrices corresponding to pure deformation (\mathbf{R}) and rotation (\mathbf{Q}), respectively. The former is intended for solving the network input arguments related to cell configuration, and the latter one provides rotation angle of a cell at a certain position, whose role is twofold: first, ‘recovering’ outputs of the NN to actual values in the practical structure (for instance, predictions of the equivalent elasticity tensor can be used to solve the homogenisation problem only if they are transformed to those at specific rotation angles); second, ‘returning’ the real structure solutions to the original values that in the cases absence of rigid body rotation (for instance, homogenised strains obtained from real macro problems can be fed into the NNs only if they have been transformed to the cell local coordinate system). The transformation of quantities involved above is expressed as:

$$\mathbb{C}_{ijkl}^H = Q_{ip} Q_{jq} Q_{ks} Q_{lt} \hat{\mathbb{C}}_{pqst}^H; \quad (70a)$$

$$\varepsilon_{ij}^H = Q_{pi} Q_{qj} \hat{\varepsilon}_{pq}^H, \quad (70b)$$

where symbol “ \wedge ” in these two relations indicates quantities given directly by the NN and Q_{ij} are components of the orthogonal matrix \mathbf{Q} .

An SVMSC here contains the gradually varying behaviour of infilled microstructures in a regular or even theoretically an arbitrary domain. If directly carrying out homogenisation in the actual configuration domain for an SVMSC with irregular boundaries will bring about great inconvenience, which is because it takes some time to establish an irregular model either by interpolating a large number of points to fit the boundary curves or reversing the control points to reconstruct the boundary represented by B-spline. Moreover, coordinates of points in space $[0, 1]^N$ are required in order to get the mapping Jacobian matrices at them. Hence in light of the aforementioned difficulties, we consider transferring homogenisation computation process for equivalent entities with various geometries to the unit space $[0, 1]^N$. For detailed information about degrees of the B-spline basis functions and coordinates of control points adopted in numerical examples, one can refer to Appendix B.

5.3.1 | Rectangular domain infilled with graded microstructure

In this subsection, an SVMSC in a regular rectangular domain of size $7 \text{ dm} \times 4 \text{ dm}$ is examined as shown in the right panel of Figure 13, its left boundary is fixed and a uniformly distributed traction of magnitude $p_1 = 100,000 \text{ N}$ is imposed on its right end along positive direction of axis x_1^e . The control points correspond to this configuration are given by Equation (B2).

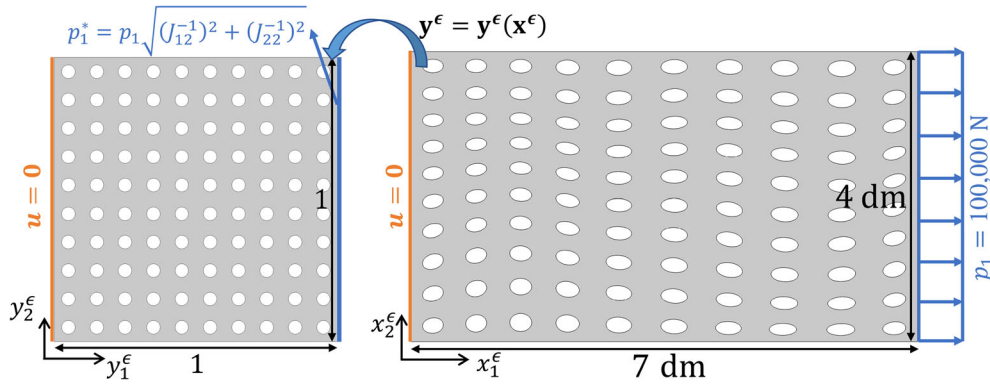


FIGURE 13 Spatially varying microstructure filled in a rectangle. BCs should be modified when considering geometry mapping operation, for instance, the external force p_1 on the right edge becomes $p_1^* = \sqrt{(J_{12}^{-1})^2 + (J_{22}^{-1})^2} p_1$ and J_{12}^{-1} and J_{22}^{-1} here represent the (1,2) and (2,2) component of the inverse matrix of \mathbf{J} .

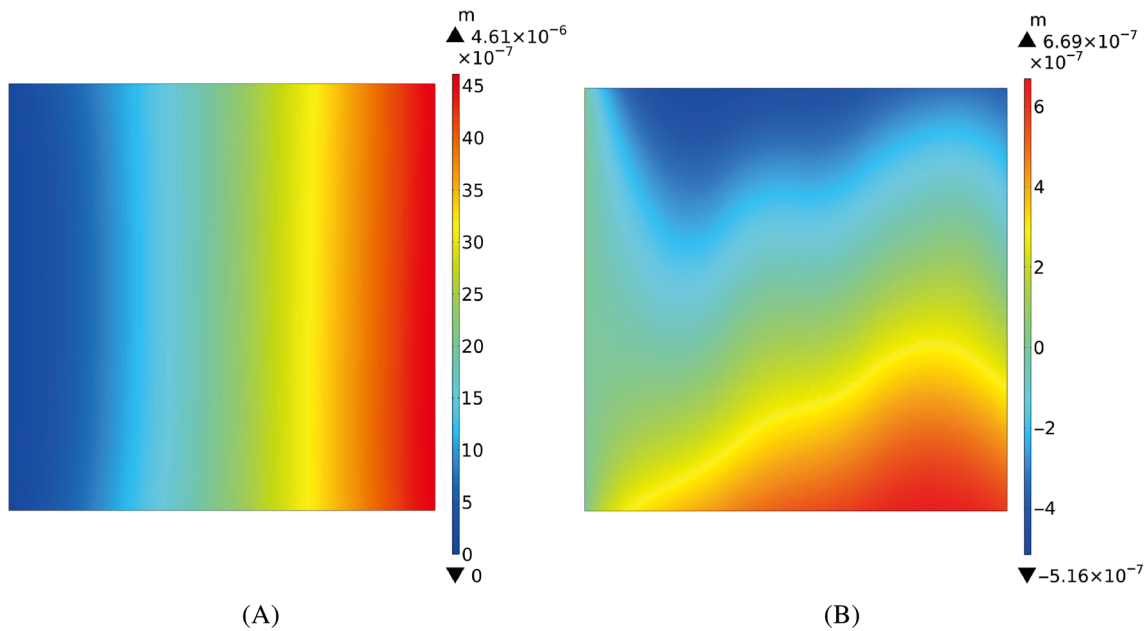


FIGURE 14 Case: Graded microstructure in a regular rectangular domain. Macroscopic homogenisation problem computed in the unit domain $[0, 1]^2$. (A) Contour plot of homogenised displacement component along the positive direction of coordinate axis y_1^ϵ ; (B) contour plot of homogenised displacement component along the positive direction of y_2^ϵ . (A) u_1^H ; (B) u_2^H .

For a two-dimensional homogenisation problem, governing equation with Jacobian operators introduced by the mapping from original equivalent entity to a unit square should be established, and the corresponding BCs should be modified. The actual elasticity tensor at each macroscopic point is obtained by substituting the output of the NN into Equation (70a), thus the original homogenisation problem can be solved equivalently in a unit square domain (see Figure 14).

Note that derivative terms of the displacements obtained here are not equal to the actual homogenised displacement gradients and need to combine the Jacobian components at a particular point to recover to the actual values. But it does not end there, such values are based on the global coordinate system, in which every unit cell has a rotation angle of its own, so the actual strain field has to be transformed to the cell local coordinate system to further serve as the input of the NN. Such a transformation relation is represented by Equation (70b).

In this example, the predictive performance of the NNs are also well investigated. From Figure 15, both the two NNs are found to present good results for the LMvMSes near the fixed structure boundary, with relative errors basically below

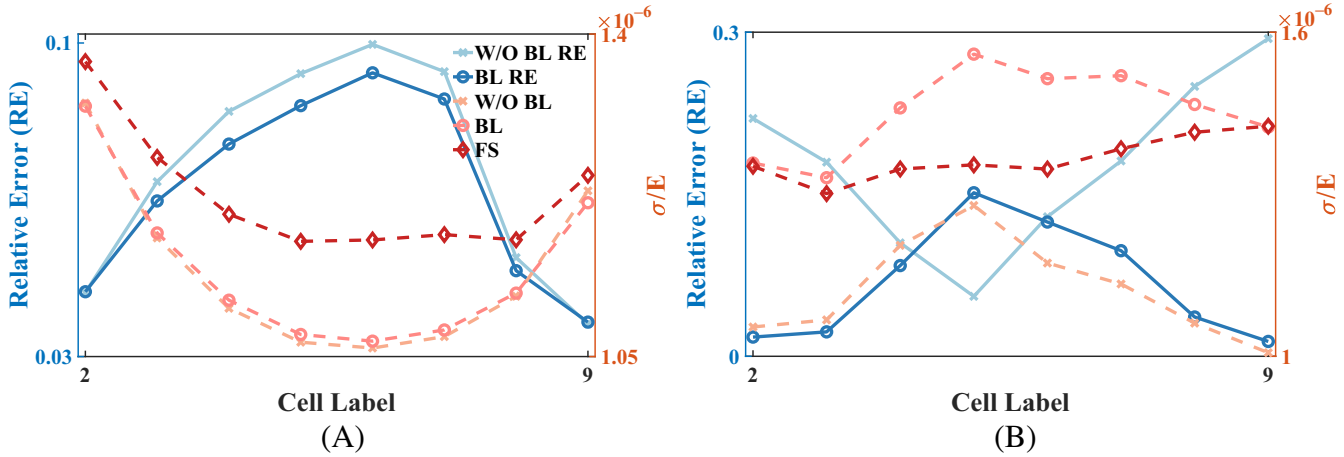


FIGURE 15 Case: Graded microstructure in a regular rectangular domain. Comparison between values predicted by the two neural networks and the benchmark obtained from direct fine-mesh finite element analysis of the multi-scale configuration.

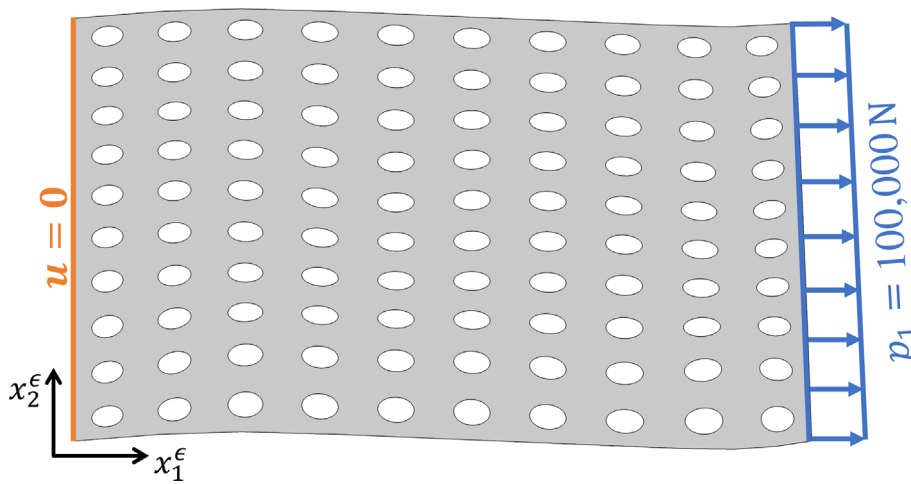


FIGURE 16 Spatially varying microstructure filled in a region bearing irregular shape.

10% (see Figure 15A), while in the case of free boundary, Figure 15B shows that the NN characterising the LMvMS in the BL demonstrates greater reliability in the LMvMS prediction.

5.3.2 | Non-rectangular domain infilled with graded microstructure

Our discussion is extended to structure where the domain boundaries become curved, as shown in Figure 16. Note that the MSC in Figure 16 is generated by transforming a periodic structure with B-spline mapping functions, and the corresponding coordinates of control points in this case given by Equation (B3). One advantage of adopting B-spline for such mapping operation is that the boundary cells stay complete no matter how the cells get distorted locally. As discussed above, even if the domain boundaries are curved (irregular), the procedure of homogenisation computation can also be implemented in the region $[0, 1]^2$ as outlined in Section 5.3.1.

Figure 17 shows the distribution contour plots of the two components of the homogenised displacement field after mapping to the unit square domain. The comparison of network performance can be seen clearly from Figure 18, from which one can draw a conclusion that the NNs constructed based on solutions for the BL problem presents predicted values much closer to the benchmark given by fine-scale results, with small relative deviations under different circumstances.

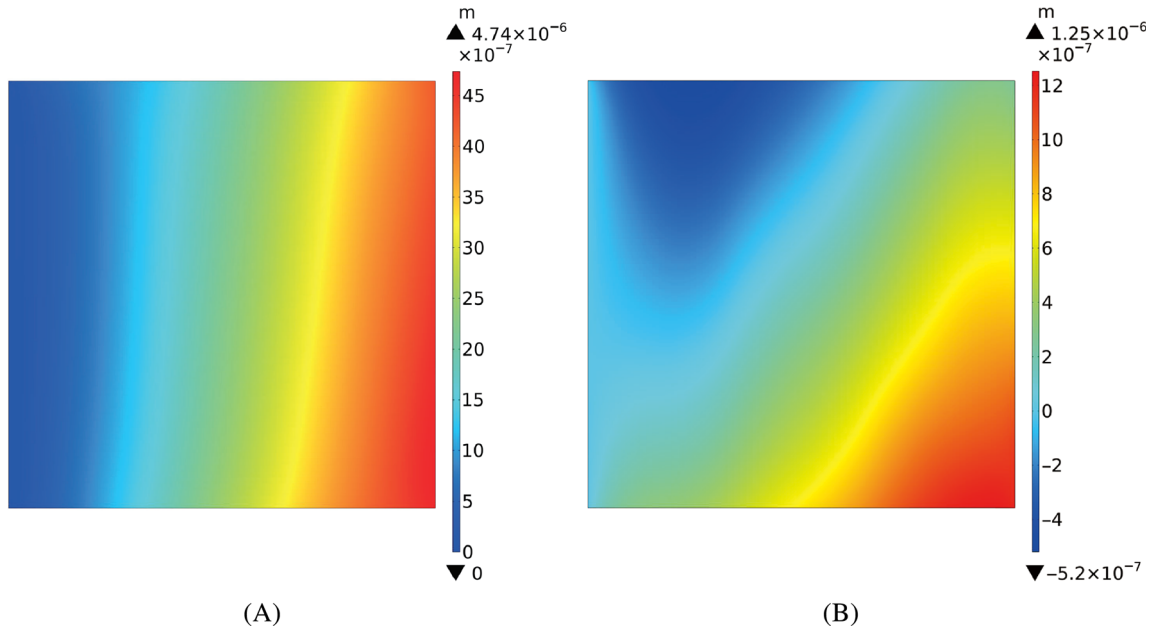


FIGURE 17 Case: Graded microstructure in a non-rectangular domain. Macroscopic homogenisation problem computed in the unit domain $[0, 1]^2$. (A) Contour plot of homogenised displacement component along the positive direction of coordinate axis y_1^e ; (B) contour plot of homogenised displacement component along the positive direction of y_2^e . (A) u_1^H ; (B) u_2^H .

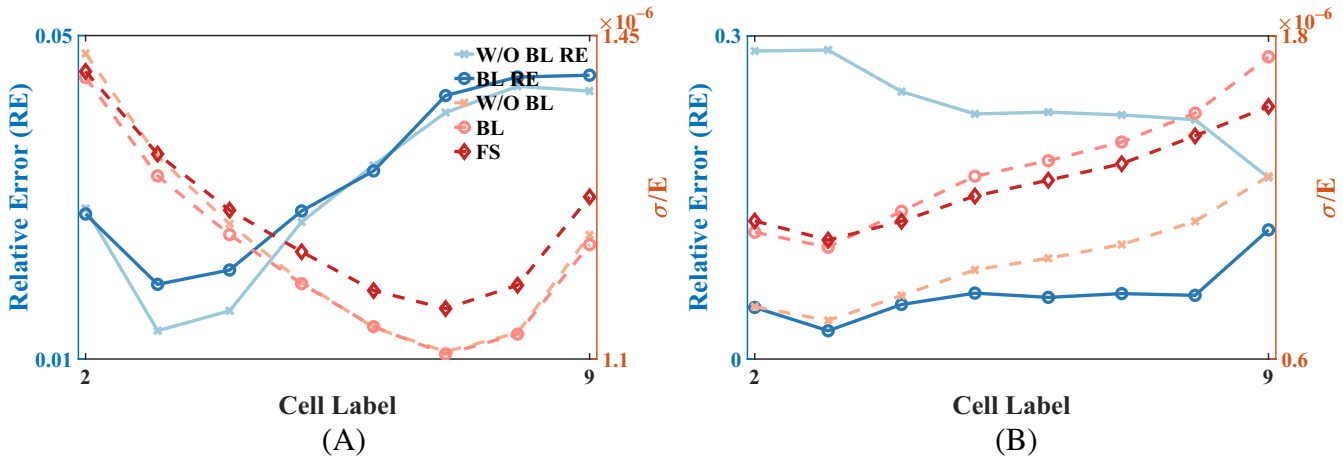


FIGURE 18 Case: Graded microstructure in a non-rectangular domain. Comparison between values predicted by the two neural networks and the benchmark obtained from direct fine-mesh finite element analysis of the multi-scale configuration.

6 | CONCLUSIONS AND DISCUSSION

In the present article, we propose a framework for analysing the boundary layer behaviour of multi-scale configurations. Combined with the use of ML, the scheme is found to accurately and efficiently capture several key local mechanical quantities, such as boundary-localised strength, in the vicinity of the overall boundary. To be more specific, the novelty here is demonstrated in two aspects.

Firstly, in a theoretical aspect (Sections 2 and 3), a new model of the BL region in the AH method is established by abandoning the original local-periodicity assumption. which presents two types of cell problems corresponding to the BL (Equations 21 and 22). We further show the surface balance equation (Equation 31), from the perspective of AH, that the homogenised displacement should satisfy on the equivalent solid surface, where the forms of the elasticity constants (Equation 30) are given by solutions for the BL cell and no longer preserve the symmetry of general fourth-order elasticity

tensor. Moreover, an later investigation on the energy of the BL region gives the surface energy (Equation 44) of an MSC, which, as seen in Equation 45, is a small quantity compared to the bulk counterpart if there is a significant contrast between the BL thickness and the structure length.

Secondly, in a computational aspect (Sections 4 and 5), it realises reliable and efficient predictions of the LMvMSes near the boundary of complex porous structures and provides the safety assessment for such configurations at the boundary. With a combinative use of the AH and ML, the original implicit relationship between the local quantity of interest and its related arguments can then be simplified to a function relation (Equation 66) that numbers in, numbers out.

Although the current framework has exhibited certain reliabilities, more accurate predictions are still in needs in some scenarios. Topics for further studies can be summarised as follows.

Firstly, the representative cells involved here are all of finite size. The solution given by the AH theory converges to the actual one only when the small parameter ϵ defined by Equation (2) is infinitesimal, thus for cells in practical porous structures, ϵ will never reach zero and the error caused by this will also never be eliminated, only reduced. The resulting truncation error is roughly of the same order-of-magnitude as ϵ .

Secondly, the contribution of surface energy is omitted in actual computation. Such a treatment is accurate as $\delta = d/L \rightarrow 0$ and may introduce a large error if δ is not small enough, however, for elliptic Dirichlet problems, the effect of BL decays exponentially as the distance from the boundary increases,³¹ therefore resulting in a tolerated error, which is roughly of magnitude $\mathcal{O}(\delta)$. For further improvement of accuracy, the surface energy term should be taken into account in the system energy functional to be minimised and the surface balance equations also need to be used instead of the real loading conditions of the homogenised solid.

Thirdly, the introduction of the B-spline does greatly endow the freedom to modify the configuration geometry, but it also brings with it the possibility of excessive local deformation, resulting in a larger gradient of the entries of the Jacobian matrices \mathbf{J} in this region compared to its surroundings. Therefore under this circumstance, the strain gradient model (higher-order theory) has to be adopted,¹⁷ that is, the material deformation or mechanical response at a point is associated with a higher-order strain gradient. So as to capture the local response, such as local stress field, more accurately, the effects of the additional terms brought by the higher-order expansion of displacement field should be carefully considered.

Finally, BL effects where inelastic effects possibly induced from singular behaviours, such as, crack initiation, etc., are present, should also be examined in depth in future.

ACKNOWLEDGEMENTS


We would like to thank the (anonymous) reviewers for the constructive suggestions. The financial supports from the National Natural Science Foundation of China (12172074, Yichao Zhu), and the Fundamental Research Funds for the Central Universities, P.R. China (Yichao Zhu) are gratefully acknowledged.

DATA AVAILABILITY STATEMENT

The data that support the findings of this study are available from the corresponding author upon reasonable request.

ORCID

Xiwei Pan  <https://orcid.org/0009-0002-8474-4498>

Zhengcheng Zhou  <https://orcid.org/0000-0001-5685-9058>

REFERENCES

1. Liu X, Furrer D, Kusters J, Holmes J. Vision 2040: a roadmap for integrated, multiscale modeling and simulation of materials and systems. Technical Report. No: E-19477, GRC-E-DAA-TN52454, NASA/CR-2018-219771. 2018.
2. Liu C, Du Z, Sun Z, Gao H, Guo X. Frequency-preserved acoustic diode model with high forward-power-transmission rate. *Phys Rev Appl*. 2015;3(6):064014.
3. Fratzl P, Barth FG. Biomaterial systems for mechanosensing and actuation. *Nature*. 2009;462(7272):442-448.
4. Aage N, Andreassen E, Lazarov BS, Sigmund O. Giga-voxel computational morphogenesis for structural design. *Nature*. 2017;550(7674):84-86.
5. Liu C, Du Z, Zhang W, Zhu Y, Guo X. Additive manufacturing-oriented design of graded lattice structures through explicit topology optimization. *J Appl Mech*. 2017;84(8):081008.
6. Suquet PM. Elements of homogenization for inelastic solid mechanics. In: Sanchez-Palencia E, Zaoui A, eds. *Homogenization Techniques for Composite Media*. Springer Berlin Heidelberg; 1987:193-198.
7. Suquet P. *Effective Properties of Nonlinear Composites: 197–264*. Springer Vienna; 1997.

8. Smit RJ, Brekelmans WM, Meijer HE. Prediction of the mechanical behavior of nonlinear heterogeneous systems by multi-level finite element modeling. *Comput Methods Appl Mech Eng*. 1998;155(1-2):181-192.
9. Feyel F. Multiscale FE2 elastoviscoplastic analysis of composite structures. *Comput Mater Sci*. 1999;16(1-4):344-354.
10. Terada K, Kikuchi N. A class of general algorithms for multi-scale analyses of heterogeneous media. *Comput Methods Appl Mech Eng*. 2001;190(40-41):5427-5464.
11. Bensoussan A, Lions JL, Papanicolau G. *Asymptotic Analysis for Periodic Structures*. Elsevier; 1978.
12. *Lecture Note in Physics* Sánchez-Palencia E. Non-homogeneous media and vibration theory. Vol 320. Springer-Verlag; 1980:57-65.
13. Fish J, Shek K, Pandheeradi M, Shephard MS. Computational plasticity for composite structures based on mathematical homogenization: theory and practice. *Comput Methods Appl Mech Eng*. 1997;148(1-2):53-73.
14. Yuan Z, Fish J. Multiple scale eigendeformation-based reduced order homogenization. *Comput Methods Appl Mech Eng*. 2009;198(21-26):2016-2038.
15. Fish J, Yu Q, Shek K. Computational damage mechanics for composite materials based on mathematical homogenization. *Int J Numer Methods Eng*. 1999;45(11):1657-1679.
16. Markenscoff X, Dascalu C. Asymptotic homogenization analysis for damage amplification due to singular interaction of micro-cracks. *J Mech Phys Solids*. 2012;60(8):1478-1485.
17. Rao Y, Xiang M, Cui J. A strain gradient brittle fracture model based on two-scale asymptotic analysis. *J Mech Phys Solids*. 2022;159:104752.
18. Zhu Y, Li S, Du Z, Liu C, Guo X, Zhang W. A novel asymptotic-analysis-based homogenisation approach towards fast design of infill graded microstructures. *J Mech Phys Solids*. 2019;124:612-633.
19. Dvorak GJ. Transformation field analysis of inelastic composite materials. *Proc R Soc Lond Ser A Math Phys Sci*. 1992;437(1900):311-327.
20. Dvorak G, Wafa A, Bahei-El-Din Y. Implementation of the transformation field analysis for inelastic composite materials. *Comput Mech*. 1994;14(3):201-228.
21. Michel JC, Suquet P. Nonuniform transformation field analysis. *Int J Solids Struct*. 2003;40(25):6937-6955.
22. Michel JC, Suquet P. Computational analysis of nonlinear composite structures using the nonuniform transformation field analysis. *Comput Methods Appl Mech Eng*. 2004;193(48-51):5477-5502.
23. Feyel F, Chaboche JL. Multi-scale non-linear FE2 analysis of composite structures: damage and fiber size effects. *Rev Eur Des Éléments Finis*. 2001;10(2-4):449-472.
24. Moulinec H, Suquet P. A numerical method for computing the overall response of nonlinear composites with complex microstructure. *Comput Methods Appl Mech Eng*. 1998;157(1-2):69-94.
25. Geers MG, Kouznetsova VG, Brekelmans W. Multi-scale computational homogenization: trends and challenges. *J Comput Appl Math*. 2010;234(7):2175-2182.
26. Lefik M, Schrefler B. FE modelling of a boundary layer corrector for composites using the homogenization theory. *Eng Comput*. 1996;13(6):31-42.
27. Zhou Z, Zhu Y, Guo X. Machine learning based asymptotic homogenization and localization: Predictions of key local behaviours of multiscale configurations bearing microstructural varieties. *Int J Numer Methods Eng*. 2023;124(3):639-669.
28. Sanchez-Palencia E. Boundary layers in thermal conduction and elasticity. In: Sanchez-Palencia E, Zaoui A, eds. *Homogenization Techniques for Composite Media*. Springer Berlin Heidelberg; 1987:137-147.
29. Dumontet H. *Boundary Layers Stresses in Elastic Composites*. Vol 12. Elsevier; 1985:215-232.
30. Devries F, Dumontet H, Duvaut G, Lene F. Homogenization and damage for composite structures. *Int J Numer Methods Eng*. 1989;27(2):285-298.
31. Lions JL. *Some Methods in the Mathematical Analysis of Systems and their Control(Book)*. Science Press; 1981.
32. He Z, Pindera MJ. Finite volume-based asymptotic homogenization of periodic materials under in-plane loading. *J Appl Mech*. 2020;87(12):121010.
33. Gao Y, Xing Y, Huang Z, Li M, Yang Y. An assessment of multiscale asymptotic expansion method for linear static problems of periodic composite structures. *Eur J Mech-A Solids*. 2020;81:103951.
34. Drago A, Pindera MJ. Micro-macromechanical analysis of heterogeneous materials: macroscopically homogeneous vs periodic microstructures. *Compos Sci Technol*. 2007;67(6):1243-1263.
35. Gurtin ME, Ian MA. A continuum theory of elastic material surfaces. *Arch Ration Mech Anal*. 1975;57(4):291-323.
36. Gurtin ME, Murdoch AI. Surface stress in solids. *Int J Solids Struct*. 1978;14(6):431-440.
37. Zhu Y, Wei Y, Guo X. Gurtin-Murdoch surface elasticity theory revisit: an orbital-free density functional theory perspective. *J Mech Phys Solids*. 2017;109:178-197.
38. Catto I, Le Bris C, Lions PL. *The Mathematical Theory of Thermodynamic Limits: Thomas-Fermi Type Models*. Oxford University Press; 1998.
39. Piegel L, Tiller W. *The NURBS Book*. Springer Science & Business Media; 1996.
40. Ma C, Xue D, Li S, Zhou Z, Zhu Y, Guo X. Compliance minimisation of smoothly varying multiscale structures using asymptotic analysis and machine learning. *Comput Methods Appl Mech Eng*. 2022;395:114861.

41. Li S, Zhu Y, Guo X. Optimisation of spatially varying orthotropic porous structures based on conformal mapping. *Comput Methods Appl Mech Eng.* 2022;391:114589.
42. COMSOL. COMSOL Multiphysics[®] v. 5.6. COMSOL AB. 2020. Accessed January 2, 2022. cn.comsol.com

How to cite this article: Pan X, Zhou Z, Ma C, Li S, Zhu Y. Machine-learning-based asymptotic homogenisation and localisation considering boundary layer effects. *Int J Numer Methods Eng.* 2023;e7367. doi: 10.1002/nme.7367

APPENDIX A. PROOF OF TRANSFORMATION BETWEEN DIFFERENT BOUNDARY ORIENTATIONS

We now prove that Equations (62a) and (62b) are correct. Relations of the solutions for the periodic cell under different scaling factors and rotation angles have been given in the case of conformal mapping,⁴¹ along this lines, the rotation of the BL cell is investigated. First of all, the components of the elasticity tensor remain the same in any reference coordinate for a configuration with isotropic base material, that is,

$$\mathbb{C}_{ijkl} = Q_{ia} Q_{jb} Q_{kc} Q_{ld} \mathbb{C}_{abcd}; \quad (\text{A1a})$$

$$\mathbb{C}_{ijk\alpha} = Q_{ia} Q_{jb} Q_{kc} Q_{\alpha d} \mathbb{C}_{abcd}, \quad (\text{A1b})$$

where \mathbf{Q} stands for an orthogonal matrix. To demonstrate the transformation of cell solutions under different rotation angles, “characteristic equations” of the two types of BL cell problems must be specified, which here indicate equations independently contain the meaning of each free index of the generalised displacement. For example, the free indices st of variable $\tilde{\eta}_k^{st}$ in the governing equation of Equation (22) do not carry any physical meaning (like prestrain) if the equation is separately examined. And the proper “characteristic equations” of BL cell problems can be derived from the discussion on generalisation in Section 3.2

$$\mathbf{J}_{mj} \frac{\partial}{\partial \bar{z}_m} \left(\mathbb{C}_{ijk\alpha} \delta_{ks} \delta_{\alpha\beta} + \mathbb{C}_{ijkl} \mathbf{J}_{rl} \frac{\partial \tilde{\xi}_k^{s\beta}}{\partial \bar{z}_r} \right) = 0; \quad (\text{A2a})$$

$$\mathbb{C}_{ijkl} \mathbf{J}_{rl} \frac{\partial \tilde{\eta}_k^{st}}{\partial \bar{z}_r} m_j \Big|_{\partial \tilde{\gamma}_c} = \left(\mathbb{C}_{ijst} + \mathbb{C}_{ijkl} \mathbf{J}_{rl} \frac{\partial \tilde{\xi}_k^{st}}{\partial \bar{z}_r} \right) m_j \Big|_{\partial \tilde{\gamma}_c}, \quad (\text{A2b})$$

$\alpha, \beta = 1, \dots, N-1$, while \mathbf{J} , which originally reflects stretching, rotating and twisting of a cell, only represents the rigid body rotation here, corresponding to $\mathbf{R} = \mathbf{I}$ in Equation (68). Thus the relationship between the Jacobian matrix and the orthogonal matrix is

$$\mathbf{J}_{ij} = \mathbf{Q}_{ji}. \quad (\text{A3})$$

Substituting Equations (A1), (A3), into Equation (A2a) gives

$$\mathbf{Q}_{jm} \frac{\partial}{\partial \bar{z}_m} \left(\mathbf{Q}_{ia} \mathbf{Q}_{jb} \mathbf{Q}_{se} \mathbf{Q}_{\beta f} \mathbb{C}_{abef} + \mathbf{Q}_{ia} \mathbf{Q}_{jb} \mathbf{Q}_{kc} \mathbf{Q}_{ld} \mathbb{C}_{abcd} \mathbf{Q}_{lr} \frac{\partial \tilde{\xi}_k^{s\beta}}{\partial \bar{z}_r} \right) = 0, \quad (\text{A4})$$

based on a relation: $\mathbf{Q}_{ji} \mathbf{Q}_{jk} = \delta_{ik}$, $i, j, k = 1, \dots, N$ for the orthogonal matrix \mathbf{Q} , we multiply both ends of Equation (A4) by \mathbf{Q}_{ip} to get

$$\frac{\partial}{\partial \bar{z}_m} \left(\mathbf{Q}_{se} \mathbf{Q}_{\beta f} \mathbb{C}_{pmef} + \mathbf{Q}_{kc} \mathbb{C}_{pmcr} \frac{\partial \tilde{\xi}_k^{s\beta}}{\partial \bar{z}_r} \right) = 0, \quad (\text{A5})$$

further consider the substitution of indices in the above equation, and the new equation is obtained by replacing the original indices p, m, c, r, k with i, j, k, l, m , that is,

$$\frac{\partial}{\partial \bar{z}_j} \left(Q_{se} Q_{\beta f} C_{ijef} + C_{ijkl} \frac{\partial (Q_{mk} \bar{\xi}_m^{s\beta})}{\partial \bar{z}_l} \right) = 0, \tag{A6}$$

For the reference BL cell, its rotation matrix is an identity matrix, so the corresponding governing equation is reduced to the form of that in periodic case. If we denote the incomplete index of the reference BL cell takes the value α , the one after rotation takes the value β , then we have the relation: when $\alpha = \beta$, $Q_{ij} = 0$, for $i \neq j$; when $\alpha \neq \beta$, $Q_{ij} = 0$, for $i = j$. A comparison between Equations (A6) and (21a) gives the following equation

$$Q_{mk} \bar{\xi}_m^{s\beta} = Q_{st} Q_{\beta\alpha} \hat{\xi}_k^{t\alpha}, \quad \text{for } \alpha, \beta = 1, \dots, N - 1, \tag{A7}$$

where “ \wedge ” indicates solutions correspond to the reference BL cell and are already known. Again, multiplying Q_{nk} at both ends of the equation and then replacing the indices $n, s, m, t, \beta, \alpha$ with $i, j, k, s, \alpha, \beta$, Equation (62a) is finally proven.

With the above process, the proof of transformation for another BL cell problem is straightforward, but two points should be stated: first, the proof here is carried out based on the ‘characteristic equation’ (Equation A2b) instead of the governing equation, second, transformation relation of the interior cell rotation should be identified $\bar{\xi}_i^{jkl} = Q_{ir} Q_{js} Q_{kt} \hat{\xi}_r^{st}$. The detailed proof of Equation (62b) is thus omitted here.

APPENDIX B. DETAILS ON SPECIFIC SETTINGS ASSOCIATED WITH B-SPLINE

The specific parameters related to B-spline mapping are listed below. A two-dimensional pattern formed by Equation (52) can be generally viewed as a net woven by two families of B-splines corresponding to two orthogonal directions, respectively. The number of control points along these two directions is: $n = 8, m = 6$ and the maximum degrees of B-spline basis functions are selected as $p = q = 2$.

In this article, ‘clamped’ type B-spline is selected as the mapping representation, in which the corresponding knot vectors are in such a form: nodes at both ends have a repeat degree of $D + 1$, D represents the maximum degree of the B-spline basis function, the rest of the nodes are uniformly distributed with a repeat degree of 1, that is,

$$U = \left[\underbrace{0, \dots, 0}_{p+1}, y_{p+1}^1, \dots, y_{n-1}^1, \underbrace{1, \dots, 1}_{p+1} \right], \quad V = \left[\underbrace{0, \dots, 0}_{q+1}, y_{q+1}^2, \dots, y_{m-1}^2, \underbrace{1, \dots, 1}_{q+1} \right]. \tag{B1}$$

For example, if the number of control points $N = 6$ and the maximum degree $D = 2$, then the knot vector $U = \left[0, 0, 0, \frac{1}{4}, \frac{1}{2}, \frac{3}{4}, 1, 1, 1 \right]$.

The coordinates of control points corresponding to the B-spline adopted in rectangular multi-scale structure in Section 5.3.1 take the form

$$\mathbf{P} = \left\{ \begin{array}{cccccccc} [0, 0] & [0.5, 0] & [1.5, 0] & [2.6, 0] & [3.8, 0] & [5, 0] & [6.5, 0] & [7, 0] \\ [0, 0.5] & [0.5, 0.5] & [1.5, 0.7] & [2.6, 0.6] & [3.8, 0.5] & [5, 0.4] & [6.5, 0.5] & [7, 0.5] \\ [0, 1.6] & [0.5, 1.6] & [1.5, 1.7] & [2.6, 1.6] & [3.8, 1.6] & [5, 1.6] & [6.5, 1.5] & [7, 1.6] \\ [0, 2.6] & [0.5, 2.6] & [1.5, 2.7] & [2.6, 2.5] & [3.8, 2.6] & [5, 2.5] & [6.5, 2.4] & [7, 2.6] \\ [0, 3.5] & [0.5, 3.5] & [1.5, 3.4] & [2.6, 3.2] & [3.8, 3.5] & [5, 3.4] & [6.5, 3.4] & [7, 3.5] \\ [0, 4] & [0.5, 4] & [1.5, 4] & [2.6, 4] & [3.8, 4] & [5, 4] & [6.5, 4] & [7, 4] \end{array} \right\}. \tag{B2}$$

The coordinates of control points corresponding to the B-spline adopted in non-rectangular multi-scale structure in Section 5.3.2 take the form

$$\mathbf{P} = \left\{ \begin{array}{cccccccc} [0, 0] & [0.5, 0.05] & [1.6, 0.1] & [2.8, 0.05] & [4, 0] & [5.2, -0.05] & [6.48, -0.1] & [6.98, 0] \\ [0, 0.5] & [0.5, 0.55] & [1.6, 0.8] & [2.8, 0.7] & [4, 0.7] & [5.2, 0.5] & [6.46, 0.7] & [6.96, 0.55] \\ [0, 1.6] & [0.5, 1.65] & [1.6, 1.7] & [2.8, 1.6] & [4, 1.6] & [5.2, 1.6] & [6.42, 1.5] & [6.92, 1.6] \\ [0, 2.6] & [0.5, 2.65] & [1.6, 2.7] & [2.8, 2.5] & [4, 2.6] & [5.2, 2.5] & [6.38, 2.4] & [6.88, 2.5] \\ [0, 3.5] & [0.5, 3.55] & [1.6, 3.6] & [2.8, 3.55] & [4, 3.49] & [5.2, 3.45] & [6.34, 3.4] & [6.84, 3.5] \\ [0, 4] & [0.5, 4.05] & [1.6, 4.1] & [2.8, 4.05] & [4, 4] & [5.2, 3.95] & [6.3, 3.9] & [6.8, 3.95] \end{array} \right\} \quad (\text{B3})$$